https://doi.org/10.5194/egusphere-2024-3
Preprint. Discussion started: 26 January 2024

Thermal-Driven Graupel Generation Process to Explain Dry-Season Convective Vigor over the Amazon

Authors: Toshi Matsui[1&2], Daniel Hernandez-Deckers[3], Scott E. Giangrande[4], Thiago S. Biscaro[5], Ann Fridlind[6], and Scott Braun[1]

[1] *Mesoscale Atmospheric Processes Laboratory, NASA Goddard Space Flight Center, Greenbelt, MD, USA*
[2] *Earth System Science Interdisciplinary Center – ESSIC, University of Maryland, College Park, MD, USA*
[3] *Grupo de Investigación en Ciencias Atmosféricas, Departamento de Geociencias, Universidad Nacional de Colombia, Bogotá, Colombia*
[4] *Environmental and Climate Sciences Department, Brookhaven National Laboratory, Upton, NY, USA*
[5] *Meteorological Satellites and Sensors Division, National Institute for Space Research, Cachoeira Paulista, São Paulo, Brazil*
[6] *NASA Goddard Institute for Space Studies, New York, NY, USA*

Correspondece to: Toshi Matsui, Toshihisa.Matsui-1@nasa.gov

https://doi.org/10.5194/egusphere-2024-3
Preprint. Discussion started: 26 January 2024

Abstract. Large-eddy simulations (LESs) are conducted for each day of the intensive observation periods (IOPs) of the Green Ocean Amazon (GoAmazon) field campaign to characterize the updrafts and microphysics within deep convective cores while contrasting those properties between Amazon wet and dry seasons. Mean Doppler velocity (V_{dop}) simulated using LESs are compared with 2-year measurements from a Radar Wind Profiler (RWP) as viewed by statistical composites separated according to wet and dry season conditions. In the observed RWP and simulated LES V_{dop} composites, we find more intense low-level updraft velocity, vigorous graupel generation, and intense surface rain during the dry periods than the wet periods. To investigate coupled updraft-microphysical processes further, single-day golden cases are selected from the wet and dry periods to conduct detailed cumulus thermal tracking analysis. Tracking analysis reveals that simulated dry-season environments generate more droplet-loaded low-level thermals than wet-season environments. This tendency correlates with seasonal contrasts in buoyancy and vertical moisture advection profiles in large-scale forcing. Employing a normalized time series of mean thermal microphysics, the simulated cumulus thermals appear to be the primary generator of cloud droplets. At the same time, ice crystals tend to be generated in inactive parts of clouds. Time series shows that thermals, however, entrain ice crystals and enhance riming due to large concentrations of droplets in the thermal core. This appears to be a production pathway of graupel/hail particles within simulated deep convective cores. In addition, less-diluted dry-case thermals tend to be elevated higher, and graupel grows further during sedimentation after spilling out from thermals. Therefore, greater concentrations of low-level moist thermals likely result in more graupel/hail production and associated dry-season convective vigor.

https://doi.org/10.5194/egusphere-2024-3
Preprint. Discussion started: 26 January 2024

1. Introduction

Deep convection is a fundamental process of turbulence that drives the Earth's general circulation and regulates thermodynamic fields (Emanuel et al., 1994). Deep convection undergoes complex dynamical and microphysical processes throughout its life cycle, which appear as towering clouds visible from satellites in different parts of the world (Stephens et al., 2002). As a result, deep convection generates significant amounts of atmospheric latent heat, surface precipitation, and hydrometeors that reflect/absorb solar and infrared radiation, modifying atmospheric circulation and surface energy and mass fluxes (Hartmann, 2016). These complexities in deep convection and feedback processes pose significant challenges in predicting weather and climate using numerical Earth system modeling across different scales (Grabowski and Petch, 2009; Sullivan and Voigt, 2021).

Characteristics of deep convection are unique in different seasons and geographic regimes affected by the local environment. One of the most straightforward yet most robust regime separation concepts is the land-ocean (L-O) contrast (Williams and Stanfill 2002). Solar radiation warms the surface skin temperature over land more readily than over the ocean due to the smaller heat capacity of soils and vegetation than deep water bodies, thus producing stronger surface infrared flux and turbulent heat flux (Matsui and Mocko 2014). This greater surface energy deepens planetary boundary layers that may trigger deeper convective clouds depending on the atmospheric profiles (Pielke 2001). Overall, the continental environment tends to promote deeper convection with stronger, wider convective cores (Lucas et al. 1994, Wang et al. 2019), with suppressed warm rain and enhanced cold precipitation process (Williams et al. 2005), which often leads to unique drop-size distribution characteristics and precipitation partitioning between convective and stratiform process outcomes in different geographic regions (e.g., Tokay and Short 1996; Giangrande et al. 2012; Dolan et al. 2018).

Satellite observations similarly depict continental convective invigoration as characterized by more frequent lightning flashes and heavily rimed particles aloft over land than ocean (Williams et al. 2004, Zipser et al. 2006, Stolz et al. 2015, Matsui et al. 2016). Takahashi et al. (2017 & 2021)

https://doi.org/10.5194/egusphere-2024-3
Preprint. Discussion started: 26 January 2024

show that continental convection generally contains less diluted cores than their oceanic counterparts, following an inverse relationship between convective core width and dilution rate. Similarly, Jeyaratnam et al. (2020) recently suggested that convective updraft and mass flux properties were distinctly different between tropical land and tropical oceanic convection using methods to estimate those properties that blend satellite observations with plume models. Hereafter, we define "convective vigor" by the enhanced cold-precipitation process characterized by larger rimed particles (graupel/hail) and vigorous raindrops in convective cores.

Representation of deep convective cloud land-ocean contrasts is still an ongoing challenge for global atmospheric models at storm-resolving resolution (a few km of horizontal grid spacing), partially owing to the poor representation of cloud dynamics (Matsui et al. 2016). Robinson et al. (2011) configured idealized simulation setups to investigate the "island" effect of convection with finer grid spacing (500 m or 1 km) and successfully simulated convective vigor equivalent to the observed microwave brightness temperature. Matsui et al. (2020) used a nested regional model with 1 km grid spacing to compare mid-latitude continental versus tropical maritime storms and successfully reproduced land-ocean contrasts of hydrometeor identification profiles from polarimetric radars.

However, statistical evaluation of simulated vertical velocity and association with convective vigor process (i.e., graupel/hail generation) have not yet been examined very well due to a lack of observations and detailed process-oriented model investigation, respectively. For example, mesoscale convective system (MCS) studies performed by Prein et al. (2022) and Ramos-Valle et al. (2023) highlight the challenges when attempting to represent continental convection within the constraints of limited observations while attempting to establish optimal configurations as a function of model grid spacing for typical midlatitude (Oklahoma) and tropical continental (Amazon) conditions.

The 2-year measurements from the Green Ocean Amazon (GoAmazon) campaign provide unprecedented data on the vertical velocity of deep convection by the Atmospheric Radiation Measurement user facility (ARM, ARM Mobile Facility (AMF), Martin et al. 2017, Giangrande et al. 2017). Recently, Giangrande et al. (2023) contrasted the thermodynamics and lifecycle

https://doi.org/10.5194/egusphere-2024-3
Preprint. Discussion started: 26 January 2024

properties, including the vertical air velocity within isolated convective clouds observed during the Amazon wet and dry seasons, and found that dry-season convection exhibited more intense low-level updrafts and stronger precipitation properties associated with smaller convective cell areas than wet-season counterparts. Dry-season convection also tended to exhibit a shorter life cycle and often achieved maximum updraft and precipitation intensity at earlier life cycle stages than wet-season storms. Pre-convective thermodynamics profiles from those events revealed that the dry season showed a stronger deficit of dew-point temperature in the middle troposphere and higher values of mean-layer convective available potential energy (MLCAPE) at lower levels.

In addition to primary thermodynamic transitions between wet and dry season convective regimes (e.g., Giangrande et. al. 2020), the Amazon dry seasons may experience larger concentrations of aerosols due to biomass burning that have been recently associated with potential secondary contributions to changes in storm precipitation properties and convective vigor (e.g., Lin et al. 2006; Wang et al. 2018; Öktem et al. 2023). Moreover, the Amazon dry (wet) season has long been suggested to promote a continental (maritime) convection contrast for a given thermodynamic profile and background aerosols (Williams et al. 2002). Typical land-ocean contrast is characterized by a "hot" continental surface (Williams and Stanfill 2002) and sea-breeze type of mesoscale dynamics due to the thermal-patch effect (Robinson et al. 2011). Thus, instead of focusing on the complex nature of land-ocean contrast or other active versus break monsoonal contrasts performed globally (e.g., Holland et al. 1986, Keenan and Carbone 1992, Pope et al. 2009, Wu et al. 2009), the dry-wet season contrasts over the Amazon basin allows a unique emphasis on the impact of thermodynamic profiles and large-scale dynamics upon the formulation of convective vigor.

The main objective of this paper is to investigate dry-wet seasonal contrast and potential changes in the evolution of deep convection cloud processes using an LES model and forward simulations of Doppler radar observations. This attempts to reveal dynamical and microphysical processes that explain the observed dry-wet contrasts, focusing on the bulk controls imposed by the background thermodynamic profiles and large-scale forcing. The motivation for these efforts is the argument that an improved understanding of these dry-wet contrasts should facilitate untangling the more complex processes of land-ocean contrasts in deep convection. For this study, we employ a series

https://doi.org/10.5194/egusphere-2024-3
Preprint. Discussion started: 26 January 2024

of daily large-eddy simulations (LESs) with bulk single-moment microphysics throughout the GoAmazon campaign dry and wet season intensive observation periods (IOPs) to characterize dry-wet season contrast in convection. These simulations are validated against the cumulative statistics collected by ground-based Doppler velocity measurements during those periods. A thermal tracking analysis is conducted to select golden cases from these dry- and wet-season LES runs to investigate the physical process of convective vigor further. This effort focuses on thermodynamic impacts and cloud dynamical roles in this manuscript, while the aerosol effects will be investigated in another study.

Section 2 describes the general methodology and tools, including radar profilers, LES, instrumental simulators, large-scale meteorological forcing, and thermal-tracking algorithms for this study. Section 3 shows the results of the dry-wet contrast of meteorological forcing, statistical composites of Doppler velocity, and thermal tracking analysis. Section 4 summarizes a thermal-driven process of dry-season convective vigor, its uncertainties, and future directions.

2. Methods

2.1 GoAmazon: RWP Observations

The primary datasets for this study are those collected by the 1290 MHz ARM Radar Wind Profiler (RWP) operated during the U.S. Department of Energy's ARM ARM facility deployment during its "Observations and Modeling of the Green Ocean Amazon 2014–2015" (GoAmazon) campaign near Manaus, Brazil, from March 2014 through December 2015 (e.g., Martin et al., 2017). The RWP was configured for precipitation sampling that included frequent vertical pointing to collect conventional radar reflectivity factor Z and mean V_{dop} profiles through deep convective cells to approximately 17 km in altitude (e.g., Giangrande et al. 2013, Giangrande et al. 2016, Wang et al. 2019, Williams et al. 2023). For measurements collected at these ultra-high frequencies and without expectations for larger hail in Amazon deep convective storms, all radar estimates are assumed as within Rayleigh scattering regimes, and measurements are unattenuated in rain. The RWP deployed during GoAmazon had a beam width of approximately 10 degrees thus horizontal

https://doi.org/10.5194/egusphere-2024-3
Preprint. Discussion started: 26 January 2024

measurement resolution is typically less than 1 km, with a 200 m vertical (bin, gate) resolution and 10-s intervals between consecutive radar profiles. All radar measurements were calibrated against a reference laser disdrometer collocated at the main AMF site during the campaign (e.g., Wang et al. 2018).

For observation and simulation comparisons, the deep convective core is defined by using thresholds applied to the observed and simulated RWP profiles: 1) column-maximum reflectivity is greater than 35 dBZ, and 2) column-maximum V_{dop} is greater than 5 m/s. The choice for these criteria is admittedly flexible, as model-vs-observed Z thresholds, in particular, are not necessarily well-posed for convective-stratiform segregation such as removing all stratiform cells (e.g., Steiner et al. 1995). Still, the additional velocity constraint afforded by the vertically-pointing RWP and statistical representation of convective and stratiform composites seems to be reasonable (not shown here), noting what is important is an attempt to apply thresholds for both observations and simulations. A slightly different threshold does not alter the conclusions. Note that events on 3/19/14, 3/20/14, and 3/23/14, as well as the 10/4/14 cases from the dry season IOP, are clear examples of Amazon mesoscale convective systems (MCSs, e.g., Wang et al. 2019). Thus, these cases have also been removed from our statistical analysis to focus on isolated convective days.

2.2 GoAmazon LES, Forcing, and Simulator

GoAmazon LES runs utilize the Goddard Cumulus Ensemble (GCE), a cloud-process model developed and improved at NASA GSFC over several decades (Tao *et al.* 2014). The GCE is driven by large-scale forcing (LSF) with cyclic boundary conditions to generate cloud dynamics and microphysics processes in Cartesian grid coordinates. No additional heat, moisture, or momentum enters the domain apart from that imposed by the LSF or solar/infrared radiative processes. In addition, GCE's anelastic dynamic core option allows faster integration of finer-resolution runs (up to 1.5~2 times) than its compressible dynamic core option.

GoAmazon LES runs use 200-m horizontal grid spacing with 512 x 64 x 128 grids (x-y-z cartesian coordinates) with a 2-second model time step. Vertical grid spacings stretch from near surface

https://doi.org/10.5194/egusphere-2024-3
Preprint. Discussion started: 26 January 2024

level (starting from 44 m) and reach 200m around 4 km level, not to exceed horizontal resolution. Thus, the domain covers a 102 km x 12.8 km area; this "narrow channel" domain setup intends to resolve three-dimensional large eddies (i.e., thermals) while minimizing computational cost in order to run LES for the entire IOPs. In terms of model physics, the 1.5-order turbulent kinetic energy (TKE) scheme is used for subgrid turbulent mixing, and the Goddard radiation scheme is used for computing radiative flux and heating (Chou and Suarez 1999 & 2001, Matsui et al. 2018). The Goddard bulk one-moment 6-class scheme (4ICE hereafter) has four ice classes and uses preset size and density mapping for snow, graupel, and hail (Lang et al. 2014; Tao et al. 2016). 4ICE successfully generated a realistic L-O contrast of convective-core hydrometeor distributions compared to polarimetric radar retrievals in the previous study (Matsui et al. 2020). Also, note that the one-moment scheme is unaffected by the background aerosol concentrations to focus on the impact of thermodynamic and large-scale forcing on convective vigor in this study.

The LSF is derived from the VARiational ANALysis (VARANAL) approach, which is a broadly accepted method for generating large-scale forcing wherein data are collected and adjusted based on the vertical integration of the atmospheric mass, moisture, dry static energy, and momentum budgets (Zhang and Lin 1997, Zhang et al. 2001, Xie et al. 2004). The VARANAL approach is applied to the GoAmazon field campaign using ERA-Interim reanalysis (Dee et al., 2011) and constrained by radar-based surface precipitation rate (Tang et al. 2016). GoAmazon LESs are run from September 2014 to 10 October 2014, defined as the dry-season IOP, and also run from 14 February 2014 to 26 March 2014, defined as wet-season IOP, as suggested by thermodynamic behaviors characteristic of larger dry and wet-season expectations, respectively (Giangrande et al. 2017, 2020). Each daily LES is initialized at 12 AM local time and integrated just for 30 hours rather than continuously integrated during the entire IOPs because the convection life cycle typically follows a strong diurnal cycle due to the solar heating cycle, excepting propagating organized convection (Tang et al. 2016, Giangrande et al. 2017, 2020). As a default setting, hourly LES outputs are used to analyze the mean seasonal behavior of LESs.

Hourly LES outputs include an additional Doppler velocity field, corresponding to an expected RWP observation through a multi-instrumental simulator, Goddard Satellite Data Simulator Unit (G-SDSU, Matsui et al. 2014a; Matsui et al. 2014b). In this study, a ground-based Doppler radar

https://doi.org/10.5194/egusphere-2024-3
Preprint. Discussion started: 26 January 2024

simulator is implemented in the model to replicate RWP observable signals. Radar backscatter is estimated from nonRayleigh calculations with a Maxwell-Garnett assumption of air-water-ice mixtures at 1290 MHz frequency, though for the RWP frequency, vertical pointing, and media type/size expectations therein, the forward modeling is more straightforward than most weather radar wavelength applications and appropriate for Rayleigh scattering assumptions. Doppler velocity is estimated using pressure-adjusted hydrometeor terminal velocities weighted by radar backscatter spectrum for each particle size distribution (PSDs). All these single scattering calculations follow the 4ICE microphysics calculation/assumptions of particle size, density, and phase for each hydrometeor species for physics consistency (Matsui et al. 2014b). Finally, simulated signals are averaged consistent with the RWP beamwidth (10 degrees). This beamwidth implies different averaging at different heights, for example, corresponding to six horizontal grids of the LESs being averaged for a representative output at the 15 km height. Overall, this beamwidth averaging smear LES-scale Doppler velocity signal statistics closer to the anticipated observed instrumental signals (Matsui et al. 2014b). However, it should be noted that the exact sampling methods are different between observations and simulations. For example, the RWP observations are vertical pointing measurements that collect profiles at 6-second ("instantaneous") intervals. In contrast, the modeled RWP signals are drawn from a domain-wide sampling of hourly LES outputs.

2.3 Thermal Tracking Algorithm

The thermal tracking method used here is described in detail by Hernandez-Deckers and Sherwood (2016), who improved the initial version used by Sherwood et al. (2013). It is an offline algorithm that uses high temporal resolution output (~1 min) from LES to identify and track coherent rising volumes of cloudy air, i.e., thermals. The algorithm first identifies all peak vertical velocities larger than 0.8 m/s that have water condensate content of at least 0.01 g/kg at every available snapshot of the simulation and matches peaks from successive snapshots to identify the available points of the trajectories of rising cloudy air parcels. A third-order polynomial is fitted to these points to reconstruct smooth trajectories and to allow a precise estimate of the ascent rate of the rising air volume at each snapshot. Notice that this ascent rate differs from the actual vertical velocity at a

https://doi.org/10.5194/egusphere-2024-3
Preprint. Discussion started: 26 January 2024

particular grid point since thermals develop internal toroidal circulations such that the peak vertical velocity at their centers is higher than the actual ascent rate of the air volume (e.g., Blyth et al. 2005; Sherwood et al. 2013). The extent of each rising air volume (the size of each thermal) is estimated assuming a spherical shape centered at its smoothed trajectory, ensuring that the average vertical velocity of the enclosed volume matches that obtained from the derivative of the trajectory. Tracked thermals must fulfill certain requirements; for example, they must be tracked for at least three time steps, their radius must be larger than twice the horizontal grid spacing, their time-average ascent rate must be at least 1 m/s, their change in size in between successive snapshots must be less than 80% of the smallest radius, and most importantly, their trajectories must be consistent with their vertical momentum budget. The momentum budget of a tracked thermal is computed from its buoyancy (obtained from the density field), the pressure gradient force (obtained by integrating the pressure field over the entire thermal's surface), a "resolved mixing term" (obtained from the convergence of vertical momentum flux across the thermal's surface), and an entrainment or detrainment contribution due to the change in size between snapshots. This allows us to compute the expected final position of each thermal based only on its initial ascent rate, which is compared with the thermal's last tracked position. The distance between the actual and expected final positions must be smaller than the average thermal diameter and smaller than 20 % of the vertical distance traveled; otherwise, the thermal is discarded. Once thermals are tracked with this algorithm, many properties can be studied based on all available model variables of interest. For example, average values for each thermal, such as ascent rate, size, altitude, entrainment rate, etc., are easily computed. Also, composites of different quantities can be obtained for different "stages" of a thermal's lifecycle. Typically, thermals exhibit one maximum ascent rate throughout their lifetime, which indicates their most vigorous phase. This time step is used as a time reference common (t=0) to all thermals to create composites of various properties at different stages of thermal lifetimes.

This thermal tracking algorithm was first used to study the main properties of cumulus thermals in simulations of transient-growing convection (Sherwood et al., 2013; Hernandez-Deckers and Sherwood, 2016) and provided strong evidence that thermals are typically small, short-lived (4-5 minutes on average), and mix vigorously with their environment. Also, Hernandez-Deckers and Sherwood (2016) showed that the spherical shape approximation is generally valid and that thermals, rather than plumes, are a more realistic building block for cumulus clouds. Hernandez-Deckers and Sherwood (2018) used this algorithm to study the mixing properties of thermals in more detail and contrast them with known parameterizations. Results from these studies have set up the stage for a deeper understanding of cumulus dynamics and for further studies that use different approaches (e.g., Gu et al., 2020; Morrison et al., 2020; Peters et al., 2020; Xu et al., 2021; Morrison et al., 2023). Recently Hernandez-Deckers et al. (2022) used this algorithm to study aerosol-deep convection interactions, highlighting the importance of the strong coupling between microphysics and small-scale dynamics in convective clouds. Here we run this tracking algorithm with the GCE model output for 5 hours starting at 1900Z (3 pm local time) on 09/07/14 (dry case) and 02/26/14 (wet case), using 1-minute interval output.

3. Results

3.1 Dry-Wet Contrast of Large-Scale Forcing

Campaign atmospheric thermodynamic profiles and the typical variability observed during GoAmazon dry and wet seasons have been previously depicted using composite radiosonde skew-T log-P diagrams (e.g., Giangrande et al., 2017, 2020, 2023). These depictions often show very similar temperature profiles between dry and wet seasons, whereas the moisture profiles indicate apparent differences, highlighting the mid-level deficit of the dew-point temperature profile in dry-season composites. Since this study utilizes LSF to drive LESs, seasonal thermodynamics and dynamics are re-characterized by the LSF (Tang et al. 2016).

In Fig. 1, we plot a time series of apparent moisture sinks (Q2), vertical moisture advection, and parcel potential buoyancy profiles with surface precipitation rate from GoAmazon LSF for the IOPs. These time series of LSF profiles are integrated and contrasted in terms of Contoured Frequency by Altitude Diagrams (CFADs, Yuter and Houze 1995) as the dry and wet season IOPs (Figure 2).

Here, Q2 is the sum of changes in moisture content, horizontal moisture advection, and vertical moisture advection (Yanai et al. 1973), balanced with net condensation rate and turbulent transport

https://doi.org/10.5194/egusphere-2024-3
Preprint. Discussion started: 26 January 2024

of moisture vertical advection. Large Q2 corresponds to a large atmospheric moisture loss due to net condensation loss (i.e., precipitation). Large Q2 is associated with intervals with heavier or more widespread surface precipitation; thus, dry-IOP Q2 and surface precipitation are typically smaller than wet IOP (Fig. 1a-b). Similarly, Figs. 1c-d shows that peaks of vertical moisture advection term coincide with those peaks in the Q2 rate. Note that the Q2 rate in tropical environments is mainly contributed by the vertical moisture advection term rather than the horizontal advection term (not shown here). More importantly, positive (red shade) vertical moisture advection of the wet IOP tends to be stretched up to higher altitude (up to 200 mb) than the dry IOP (up to 600 mb) in most cases.

As previously discussed by Tang et al. (2016), the associated Amazon Q2 CFADs show the largest positive Q2 between 700 and 400 mb, while the largest negative Q2 is around 800 mb (Figs. 2a-b). The Dry-wet composite CFAD highlights more frequent positive Q2 values above the 800 mb level during the wet IOP. In contrast, more frequent negative Q2 during the dry IOP (Fig. 2c). Vertical moisture advection depicts similar CFAD shapes (Figs. 2d-e). Still, it highlights high frequencies of low-level positive vertical moisture advection and mid-to-low-level negative moisture vertical advection in the dry IOP in comparison with the wet IOP.

Finally, in Figs. 1e-f we plot the time series of parcel potential buoyancy profiles (positive components only), computed from LSFs by lifting surface airmass dry and moist adiabatically. These potential buoyancy magnitudes are not necessarily associated with precipitation intensity. Potential buoyancy CFADs show peak forcing between the 600 mb and 200 mb levels (Figs. 2g, h, & i). The wet IOP suggests a larger variability of potential buoyancy at the upper troposphere than the dry IOP (Figs. 2g-h). Potential buoyancy appears to be slightly stronger in the dry IOP, and concentrated in a relatively lower troposphere than its wet IOP counterpart (Fig. 2i), which agrees with findings in Giangrande et al. (2023). These results will be further discussed along the thermal concentrations in the latter section.

3.2 Dry-Wet Composite of Doppler Velocity CFADs

https://doi.org/10.5194/egusphere-2024-3
Preprint. Discussion started: 26 January 2024

Giangrande et al. (2023) highlighted dry-wet seasonal characteristics of storm vertical air motions retrieved using RWP. They found that daytime isolated dry season convective cells tend to have stronger updrafts at altitudes below the melting level. Yet, unlike their wet-season counterparts, updrafts do not increase in intensity much above the melting layer. However, dry-season convective cores were also characterized by stronger downdrafts at all altitudes, especially when compared to wet-season counterparts aloft. Our present study utilizes similar direct measurements of the mean V_{dop} from RWP to characterize the dry-wet contrast of deep convective cores. The advantage of using V_{dop} measurements is that the quantity is the direct radar measurement and helps reduce uncertainties from retrieval assumptions, such as requiring hydrometeor identification or associated terminal fall speed corrections if the intent was to retrieve the vertical air motion (Giangrande et al. 2013, 2016). Here, vertically-pointing V_{dop} measurements contain sufficient information to evaluate storm characteristics, with the understanding that these measurements represent the terminal velocities of hydrometeors combined with the vertical air motion.

In Fig. 3a, we provide the cumulative sample numbers of CFADs (for each bin of V_{dop} and altitude) as simulated and subsampled from the LES hourly outputs from the combined dry and wet season IOPs. If the sampling numbers are normalized for each altitude, this will form the V_{dop} CFADs to follow. Fig. 3b shows the sum of hydrometeor mass concentrations from each V_{dop}-altitude bin. Namely, each hydrometeor mass concentrations from "cloud", "rain", "graupel-plus-hail", or "ice-plus-snow" are separately accumulated for each bin. The larger number of samples associated with a larger accumulated mass concentration of hydrometeor can generate the "representativeness" of the hydrometeor class for a given V_{dop}-altitude bin location.

As mentioned above, we defined four regimes based on the accumulated mass of each hydrometeor category. The "cloud" category (CL) is centered around -5 m/s of V_{dop} and 4 km altitude, slightly overlapping with other categories. A "rain" category (RA) is more narrowly concentrated around -8 m/s of V_{dop} and below 4 km altitude. The "graupel-plus-hail" category (GH) is centered around -14 m/s of V_{dop} at 5 km altitude. Finally, an "ice-plus-snow" category (IS) is narrowly concentrated along -1 m/s of V_{dop} above 5 km altitude. These locations roughly correspond to each hydrometeor category's altitude and terminal velocity when factoring in the background/ambient vertical air

https://doi.org/10.5194/egusphere-2024-3
Preprint. Discussion started: 26 January 2024

velocity. Note that our "cloud" regime has no terminal velocity in GCE 4ICE microphysics, thus V_{dop} represents or tracks the background vertical air velocity and overlaps with the other regimes. Moreover, simulated V_{dop} and hydrometeor statistics are also sensitive to model physics and those assumptions to some degree. For example, any real-world cloud regime may be extended to higher altitudes, but the model 4ICE microphysics scheme tends to quickly convert cloud liquid to cloud ice category due to saturation adjustment (See Figs. 14-16 of Matsui et al. 2023). Nevertheless, this representative mapping will help discuss the variability of the V_{dop} CFADs between the dry and wet season IOPs.

In Fig. 4, we provide an observed and simulated climatology of V_{dop} CFADs as sampled from deep convective cores and summarized over the dry and wet season IOPs. In both the dry and wet season IOPs, the observed CFADs depict a smoother transition of the V_{dop} at the freezing level into the melting layer (4-5 km, Figs. 4a-b). At the same time, simulations show a more abrupt transition around the freezing layer (Figs. 4d-e). This is primarily because bulk single-moment microphysics more abruptly converts solid to liquid phases through autoconversion than explicit bin-resolving microphysics (Iguchi et al. 2014). This rapid conversion also overestimates the terminal velocity of raindrops near and just below the freezing level.

The CFADs have been summarized according to dry and wet season IOPs to explore these seasonal contrasts between the deep convective cores (Figs. 4c, 4f). In the R regime (green box), the dry IOP suggests more prevalent samples in strongly negative V_{dop} for our observations and simulations, indicating that deep convective cores during the dry season IOP tend to have more vigorous, faster-falling (larger) raindrops. In the GH regime (purple box), the dry season IOP dominates the sampling. The observations indicate this dominance (red shade) up to 10 km altitude (the extent that observations were included), while the simulation shows this behavior up to 8 km, suggesting LES underestimation in graupel/hail altitudes. In the CL regime, the observations and the simulations agree well, except that some sampling is overwhelmed by the dry season IOP behaviors in the overlapped area. This likely indicates a shift in the presence of stronger low-level updraft velocities, consistent with the analysis in Giangrande et al. (2023).

https://doi.org/10.5194/egusphere-2024-3
Preprint. Discussion started: 26 January 2024

When considering the IS regime, there are examples of agreements and discrepancies between the observations and simulations. One key agreement is that the wet IOP dominates the samples in the area of positive V_{dop} above 8 km altitude. This indicates that observations and simulations suggest a shift towards stronger upper-level vertical air velocity for the wet season IOP examples than for the dry season IOP. As before, this is consistent with the absence of dry mid-levels and the stochastic updraft model expectations from Giangrande et al. (2023). On the other hand, the observations indicate a more dominant sampling of velocities during the wet season IOP at around -3 m/s of V_{dop}, whereas simulations change the dominant sampling mode from wet to dry IOPs at around 7 km altitude. This is a potential bias in single-moment bulk microphysics, which tends to glaciate cloud droplets or raindrops more quickly into ice particles than double-moment schemes (e.g., Fig. 16 of Matsui et al. 2023). The observed composite also shows more dry-season dominant frequencies in GH zones than the simulation, indicating the underestimation (overestimation) of raindrop/graupel (ice/aggregate) particles above 7 km height.

Excepting this discrepancy in the IS regime, dry-wet composites of V_{dop} CFAD agree well between observations and simulations, suggesting that LES could successfully represent the important nature of dry-wet contrast, i.e., dry-season convection tends to generate stronger low-level updraft velocity, generating more graupel/hail, and vigorous raindrops accompanied with stronger low-level downdraft than the wet season.

To further investigate these seasonal shifts in core properties, golden cases are selected to analyze deep convection lifecycle and processes. Namely, we select two single-day simulation cases representing typical dry and wet-season convection. For this, the V_{dop} CFADs are constructed for each day during the wet and dry season IOPs, and these daily CFADs are compared to the composites of seasonal CFADs (not shown here). After day-to-day analysis of correlation and root-mean-square errors between daily and seasonal CFADs, the convective event on the 2/26/14 case is selected to represent the wet IOP convections. In contrast, the 9/7/14 case is chosen to represent dry IOP convection. Fig. 5 shows a dry-wet composite of V_{dop} CFAD using these two case studies. This figure compares quite well with the seasonal composite of V_{dop} CFAD, having the dry convective vigor signals and model biases of the seasonal composite (Fig. 4f).

https://doi.org/10.5194/egusphere-2024-3
Preprint. Discussion started: 26 January 2024

In Fig. 6, we show a time series of domain-mean profiles of convective cores drawn from these dry- and wet-season golden cases, highlighting from 1600Z (1200 local time) of the starting day to 0400Z (0000 local time) of the next day. The dry season golden event shows a clear diurnal convection cycle, peaking at 2100-2200Z (local 5-6 pm). In contrast, the wet season golden event shows an already ongoing, continuous sequence of deep convection with several embedded strong pulses. Convective top heights reach up to 17 km for both the dry and wet events (Figs. 6a-b). Low-level positive upward vertical velocity is more ubiquitous in the dry case, while upward vertical velocity of the wet case extends to the middle-to-upper troposphere up to 15km (Figs. 6c-d).

Dry-case graupel-plus-hail (GH) mass concentrations peak around 2100-2300Z when the convective clouds reach their deepest cloud top heights, and the maximum GH concentration exceeds that of the wet case. Rain mass concentrations peak between 2200Z and 00:30Z on the subsequent day for the dry case, and this appears to be slightly more intense than the rainfall simulated for the wet cases. Note that precipitation areal fraction is expected to be larger for the wet season (i.e., Giangrande et al. 2016, 2023), such that dry-season convection is often characterized by narrow yet intense isolated convection, while wet-season convection is characterized by widespread moderate to deep convection (although with higher domain mass flux). The intense surface rainfall rates are generally correlated with the generation of graupel, frozen drops, and/or small hail particles during the dry-season convection, but there are some time lags from 21Z to 22:50Z in the dry-case convection. This is because the initial convective core is much narrower, and near-surface relative humidity is slightly low (~80%) around 21Z, and later convective area increases so as near-surface relative humidity (~96%) around 21:50Z. Thus, more surface rain evaporation likely suppresses surface precipitation during earlier convective periods. These time series behaviors are generally consistent with the observed characteristics in the time-integrated V_{dop} CFADs (Fig. 5).

One key question is why larger or heavily rimed particles tend to be preferentially generated in dry-season convection compared to wet-season convection, given that both seasons indicate convection with intense updraft velocity. This question follows previous efforts of Williams and Stanfill (2002) for simulations of deep convection that contrasted land and oceanic clouds. For

https://doi.org/10.5194/egusphere-2024-3
Preprint. Discussion started: 26 January 2024

example, while land and ocean environments may have similar convective available potential energy (CAPE), differences in detailed potential buoyancy and vertical velocity profiles enable additional graupel/hail particles to form in continental deep convection when compared to the maritime environments (Matsui et al. 2020). A Lagrangian tracking analysis is performed to examine this question for Amazon dry and wet season contrasts to investigate the dynamics and microphysics within cumulus thermals for these dry and wet golden events (Section 3.3).

3.3 Thermal Tracking Analysis

Thermal tracking analysis (Section 2.3) was conducted over 5-hour periods from 1900Z to 0000Z for the dry and wet season events using 1-minute LES outputs. Fig. 7 depicts normalized x-z cross-sections of thermal properties at the moment of maximum vertical velocity in the dry and wet cases and dry-wet differences. Thermals typically experience development and decaying stages in their lifetime. During development, moist thermals increase their vertical velocity and size by releasing latent heat and entraining surrounding air (Morrison et al. 2021). After defining and tracking each thermal from the LESs, our normalizing procedure first defines the reference time from each thermal's lifetime based upon peak vertical air velocity (denoted as thermal maxima) and then conducts a weighting average of each thermal property at the thermal maxima only. Our weights are based on the magnitude of thermal mass flux to avoid under-representing properties of less-populated but vigorous thermals. Because these heights at thermal reference time are different for each thermal in dry and wet case studies, averaging properties are somewhat biased toward thermal vertical distributions (discussed later).

For example, in Fig. 7a we plot the weighted-average peak vertical air velocity (W) for the dry-case thermal (9.6 m/s) and the wet-case thermal (10.6 m/s). Perhaps surprisingly, the flux- and radius-weighted average dry-case thermal is slightly slower in W than that found for the average wet-case. Here, we find that the vertical air velocity of the wet-case thermal is more homogeneously distributed than its counterpart for the dry-case thermal, leading to higher weighted-mean W despite weaker values at thermal centers (red shade in Dry-Wet plot, Fig. 7a). Also, unexpectedly, supersaturation and cloud droplet mixing ratio (Qc) of the dry-case thermal

https://doi.org/10.5194/egusphere-2024-3
Preprint. Discussion started: 26 January 2024

are elevated compared to the wet-case thermal (Fig. 6b-c), since wet-case thermals may be expected to instead have higher supersaturation and/or more condensation owing to the higher availability of water vapor (e.g., Giangrande et al. 2023).

Exploring the other classes, the rain mixing ratio (Qr) is similar between the dry-case and wet-case thermals (0.17 g/kg), but graupel-hail concentrations (Qg+h) are significantly larger in the dry-case thermals (0.95 g/kg) compared to the wet-case thermals (0.79 g/kg); this latter result is consistent with previous discussions from event time-series in Fig. 6e. Cloud ice and snow mixing ratio (Qi+s) values are slightly larger in the wet-case thermal (3.5 g/kg) than in the dry-case thermal (3.2 g/kg). While this difference is not significant, this is also potentially a surprising outcome since dry-case deep convective clouds might otherwise be expected to be deeper/stronger and thus characterized by additional ice hydrometeor concentrations. However, some absence of these media may be partially explained by following Giangrande et al. (2020; 2023) suggestions that drier mid-to-upper levels in the dry season may limit periphery precipitation aloft (i.e., enhanced evaporation). Overall, Qr and Qg+h seem to be concentrated in these composite averages downward from the thermal core due to the gravitational sedimentation process. Supersaturation and Qc, however, are also more vertically elongated than thermal properties established by Hernandez-Deckers et al. (2022) using the Weather Research and Forecasting (WRF) model for a case of scattered convection over Houston, Texas. Qi+s is more homogeneously distributed across the defined borders of thermals. Also, dry-wet differences show slight asymmetric results, particularly in W, Qr, and Qg+h. These could be attributable to differences in horizontal wind shear, evidenced by a greater tilt in the thermal centerline flow in the dry case (gray streamlines), leading to greater concentrations in the tilt direction of more rapidly sedimenting quantities that are formed within thermals (i.e., Qr and Qg+h); since thermal composites are not aligned with the mean wind, such preferential outflow may not be fully captured by this analysis (i.e., asymmetric signatures could be greater or lesser along other directions than X alignment).

An initial leading question is why the dry-case thermals have greater cloud water and supersaturation on average. To further untangle these results in Fig. 7b-c, we derive the vertical profiles of flux-weighted mean thermal states, now including all thermal times (Fig. 8a-f). Immediately, these plots reveal striking differences between the thermal number concentration

https://doi.org/10.5194/egusphere-2024-3
Preprint. Discussion started: 26 January 2024

(N) profiles for dry-case and wet-case examples (Fig. 8a; the number of thermals per km height within the 102 km x 12.8 km domain). For instance, dry-case convection shows a larger concentration of thermals below the 8 km height, while wet-case convection promotes a more homogeneous thermal concentration that extends across most heights. This behavior is somewhat reminiscent of the distribution for the difference in vertical moisture advection and potential buoyancy profiles between the parent dry and wet season conditions (e.g., Fig. 1 and 2, discussions in Section 3.1). Moreover, thermal generation in our LES responds to these terms partially from the seasonal large-scale forcing.

According to the classic similarity theory of Morton et al. (1956), the width of thermals should increase with increases in the boundary layer depth (William and Stanhill 2002). For the Amazon basin, previous GoAmazon studies such as Giangrande et al. (2017, 2023) showed that dry season boundary layer height is generally deeper than that of the wet season, potentially on the order of 200 m deeper for isolated deep convective events they tracked. Following this logic, dry-case convection may anticipate larger thermals. However, LES thermal tracking analysis suggests that the sizes (R) of thermals upon initiation appear to be quite similar between the wet and dry events and then appear to grow at similar rates for several km before the dry-case thermal size catches up with the moist size around 6 km in height, only to be overtaken again by the deeper wet-case thermals around 9 km (Fig. 7b). This result implies that differences in moist convection between dry and wet cases are perhaps better characterized by thermal numbers rather than thermal sizes.

Qc in thermals also shows very similar profiles between the dry and wet cases (Fig. 8c). However, because thermal numbers of the dry case are more concentrated at the lower troposphere (Fig. 8a), all-height mean properties of dry-case thermals are characterized by more Qc (Fig. 7c). Qr of the wet case is nearly twice as large as the dry case (Fig. 8d); however, normalized x-z cross-section (Fig. 7d) does not show such a large difference (explained below). Qi+s also shows similar distributions (Fig. 8e). Still, total x-z mean Qi+s is larger in the wet case than the dry case due to larger thermal numbers in the upper troposphere (Fig. 7e). Uniqueness appears in thermal Qg+h (Fig. 8f). While both dry and wet cases show similar magnitude of the peak values (~0.9 g/kg), the peak height in the dry case is approximately 3 km higher than the wet case.

https://doi.org/10.5194/egusphere-2024-3
Preprint. Discussion started: 26 January 2024

Fig. 8g-j displays these hydrometeor mixing ratios averaged over the same periods, including all convective grids defined by vertical velocity greater than 1 m/s. Vertical profiles and dry-wet differences are similar to the results in Fig. 6. However, compared with the in-thermal profile results (Fig. 8c-f), it facilitates understanding of the convective core microphysics process. First, mean in-thermal convective-grid hydrometeor concentrations are smaller than in-thermal profiles; particularly in-thermal Qc values are roughly six times larger than convective-grid average Qc (Figs. 8c & 8g), suggesting that thermals are major cloud droplet generators (Hernandez-Deckers et al. 2022).

The convective-grid Qg+h of the dry case is nearly twice as high as that in the wet case, peaked around the melting layer (Figs. 8f & 8j), whereas in-thermal Qg+h shows similar peak values between the dry and wet cases. As indicated by Fig. 7f, these larger and heavier rimed particles sediment from thermals and further collision with ice and supercooled liquid must enhance the graupel growth during the sedimentation process, as suggested from aircraft measurements (Blyth and Latham 1993). Thus, elevated in-thermal Qg+h in dry-case convection can have further riming growth after falling out from thermals. This vigorous growth of Qg+h in dry-case convection eventually generates vigorous raindrops after the melting process. This is why convective-grid Qr in the dry case is larger than that in the wet case (Fig. 8h), opposite from the result of in-thermal Qr (Fig. 8d). Thus, in-thermal Qr values are not directly related to total Qr in the convective core (or surface precipitation rate) because of this cold precipitation microphysics process in deep convection.

Now, a second leading question is why the height at the peak value of dry-case in-thermal Qg+h is more elevated than the wet-case thermal (Fig. 8f). Fig. 9 shows histograms of thermal properties from the dry and wet cases. Consistent with the mean vertical profiles (Fig. 8a), more thermals are initiated below 7 km in the dry case than in the wet case (Z0, Fig. 9d). Thermal radius in the wet case is also larger than the dry case regardless of shallower boundary layer depths in the wet case (Fig. 9a), consistent with R in thermal vertical profiles reaching larger sizes at most elevations in the wet case (Fig. 8b). However, here we see that thermal vertical velocity (W, Fig. 9b), travel distance (dZ, Fig. 9c), and lifetime (Fig. 9e) in the dry case are all greater than in the wet case. Thermal entrainment rate is smaller in the dry case than the wet case. These results indicate that

https://doi.org/10.5194/egusphere-2024-3
Preprint. Discussion started: 26 January 2024

the thermals in the dry-case deep convection can travel longer distances with an extended lifetime due to a lesser dilution.

Giangrande et al. (2022) suggest that the convective area is smaller in dry-season convection over this region. Thus, this indicates that stronger low-level buoyancy in dry-season environments can more narrowly concentrate updraft and low-level thermals in the area, thus creating less diluted environments probably due to the impact of thermal drag (Romps and Charn 2015). Takahashi et al. (2022) investigated cloud-scale entrainment between continental and maritime environments and found a larger dilution rate in maritime convection than in continental convection. Our results suggest that this difference in cloud dilution happens from the thermal-process level. These conditions elevate dry-case thermals and graupel peak concentration toward higher altitudes than the wet-case convection (Fig. 7f), leading to greater graupel production.

Finally, time series of thermal properties in the x-z cross-section are constructed for the dry case. For this, each thermal at its maximum w value is centered and defined as the time of zero, and prior (later) steps are represented in negative (positive) time steps. Because of the 1-minute LES output, the time series from -3 to 3 encompasses 7 minutes of time steps. This averaging process also weighs upon the magnitude of the thermal mass flux (Hernandez-Deckers et al. 2022); thus, thermals at larger values in positive and negative time steps tend to have lesser sampling numbers. Also, to make the composites, equal-sized thermals are sampled to characterize the mean time series of thermal properties, avoiding sampling too small thermals, which often has no supersaturation (Hernandez-Deckers and Sherwood. 2016). This normalizing procedure ends up with the result that maximum W values do not appear at reference time (t=0), but better capture the evolution of the largest flux-bearing thermals (Fig. 10). We also note that a typical thermal travel distance is 1.3 km (Fig. 9c) and a minority of dry-case thermals therefore contain either no ice phase (Fig. 8e-f) or no liquid phase (Fig. 8c-d), but most contain both phases between 3 and 7 km. Note that this flux-weighting is the one way to present the results, while simple non-weighting averaging can also show similar results.

In the dry case (Fig. 10), within thermals that experience an extended peak in W (6–11 m s^{-1}), the average supersaturation, cloud, and rain mixing ratio peaks at the earlier steps and decreases

https://doi.org/10.5194/egusphere-2024-3
Preprint. Discussion started: 26 January 2024

toward the end of the time steps. This indicates that a chunk of condensation heating is the main initial driver of moist thermal growth. These thermal properties are typically centered around the thermal core. By contrast, Qi+s properties are more homogeneous and less concentrated at the core of thermals, and they tend to increase toward the end of the time series. Especially, the early stages (t=-3, -2, & -1) indicate thermals are approaching an existing ice layer rather than generating ice around the thermal core. In the later stages (t=1, 2, & 3), the Qi+s is weakly concentrated toward the upper thermal cores. This evolution of Qi+s suggests that thermals are not the main initiator of Qi+s, while Qi+s is rather entrained into the thermal within the early stages of the mixed-phase zone, at least using the single-moment bulk microphysics. On the other hand, after liquid saturation is no longer contributing substantially to Qc, Qi+s becomes a leading destination of the overall transfer from vapor to hydrometeor phases within thermals that remain vigorous. This also suggests that the glaciation process (i.e., conversion from supercooled liquid to ice hydrometeors) is usually completed after thermals vanish unless they reach the upper level of convective cores.

On the other hand, Qg+h increases toward the peak time of thermals (t=0), and starts decreasing toward the later time steps (t=3). The spatial concentration of Qg+h is also peaked around the thermal cores, similar to W, rh, Qc, and Qr. The increase of Qg+h coincided with the timing of thermal entrapment of Qi+s and a reduction in Qc and Qr for time steps between -3 and 0. This suggests that large concentrations of in-thermal Qc and Qr collide with entrained Qi+s to enhance the riming process, generating graupel and hail particles. After the reference time step (t=0), Qg+h decreases, most likely due to sedimentation exceeding production. As indicated by Fig. 8f & 8j, this spilled graupel and hail can further grow by colliding with supercooled liquid and ice particles until melting. Taken together, this analysis also suggests that this vigorous Qg+h-generation process in the convective core *does not* occur through the classic parcel-driven convection; i.e., a large single air mass lifted from the cloud base up to the cloud top can generate latent heat and precipitation (Arakawa and Schubert 1974). Instead, these graupel and hail generations are most likely driven by sequential interactions of thermal ensembles and microphysical processes. Note that the time series of the wet case also shows a similar finding but is biased toward the thermals in the upper atmosphere (not shown here).

https://doi.org/10.5194/egusphere-2024-3
Preprint. Discussion started: 26 January 2024

4. Conclusion: Thermal-driven Convection Invigoration Process

We have investigated seasonal differences of the measured and simulated V_{dop} between the dry and wet seasons to confirm dry-season convective vigor associated with enhanced cold precipitation (graupel and hail) processes. Tracked thermal properties from the selected case studies reveal unique updraft microphysics processes in the convective core that explain the dry-wet contrast in deep convection. To summarize our findings in graupel-hail development sequences, a thermal-driven process is proposed in the following steps (Fig. 11a).

1. Where condensation may occur within moist turbulent structures in the lower atmosphere, local moist thermals may be initiated, which are characterized by dipole vortex rings with intense vertical velocity, supersaturation, cloud droplets, and raindrops around the thermal core.
2. When moist thermals penetrate the 0°C isothermal layer and dissipate in the mixed-phase zone, cloud droplets are detrained and gradually glaciated to form ice-particle layers.
3. As additional thermals fill with droplets and penetrate the glaciated mixed-phase zone, they entrain ice particles and collide with each other, generating graupel and hail embryos.
4. Once graupel and hail particles grow sufficiently large, they start falling out from thermals and develop further by collecting supercooled droplets and ice particles during sedimentation.

The process of generating ice layers (Step 3) could be the largest source of uncertainty in this study. To prove the convective vigor process, this study used the simple bulk single-moment microphysics parameterization (Lang et al. 2014, Tao et al. 2016). This parameterization tends to convert droplets into ice particles through the saturation adjustment process. Cloud droplets are glaciated much more quickly when compared to two-moment microphysics (e.g. Matsui et al. 2023). Time series data also shows some ice generation near the thermal core in later lifecycle stages, which may be associated with homogeneous freezing, vapor deposition or riming. Yet, ice crystal formation processes remain one of the largest sources of microphysics uncertainty (Kanji et al. 2017; Korolev and Leisner 2020) and need further investigation to establish and adequately parameterize. Furthermore, updrafts passing through the melting layer containing both large drops and ice crystals (which are identified here as a source of graupel) have also been pinpointed as a leading source of secondary ice production in oceanic convection sampled extensively via aircraft (Korolev et al. 2020). Thus, all quantitative components of the proposed ice-graupel generation process described here remain uncertain and subject to future investigations via instrumental observations and more detailed numerical simulations.

Nonetheless, building on the ability of existing knowledge and simulations to reproduce some basic features of observations during GoAmazon, Fig. 11b shows a newly proposed process that can explain why dry-season convection has more graupel and intense precipitation than wet-season counterparts in the following steps.

1. Dry-case (wet-case) convection tends to generate more (less) numbers of droplet-loaded thermals from the lower atmosphere because of larger potential buoyant energy at a low level in the dry season.
2. Once an ice layer is built from initial cumulus thermal ensembles (Fig. 11a), more (less) numbers of droplet-loaded thermals penetrate ice layers to generate more (less) graupel and hail embryos in dry-case (wet-case) convection.
3. Individual dry-case (wet-case) thermals can rise to higher (lower) elevations via weaker (stronger) dilution, elevating in-thermal graupel at higher (lower) altitudes.
4. During sedimentation, graupel in dry-case (wet-case) thermals has a higher (lower) chance to grow due to the longer (shorter) distance toward the melting level.

The "hotter" surface in the dry season must be the physical origin of step 1, similar to L-O contrast (William and Stanfill, 2002). The dry season typically has clearer skies, less soil moisture, and stronger surface heating, leading to more turbulent heat flux and energy at the lower troposphere even during GoAmazon experiment (Biscaro et al., 2021; Ghate and Kollias, 2016). In contrast, the wet season is characterized by frequent precipitation and increased release of atmospheric latent heat with the weak surface sensible heat flux caused by wet soil moisture (Rocha et al., 2004). As a result, the entire troposphere experiences upward motion during the wet season, unlike its dry season counterpart (Tang et al., 2016).

https://doi.org/10.5194/egusphere-2024-3
Preprint. Discussion started: 26 January 2024

Contrary to the speculation made by William and Stanfill (2002), it has been found that stronger surface heating and deeper PBL during the dry season do not increase the thermal "size" based on the classic similarity theory of Morton et al. (1956). Instead, our analysis of simulations indicates that the "numbers" of cumulus thermals become more important, particularly those initiated in the lower troposphere. Even for similar CAPE, the concentration of potential buoyancy profiles in the lower troposphere can trigger more vigorous convection. This is similar to the difference between mid-latitude continental and tropical maritime environments, where the mid-latitude continental environment tends to have more potential buoyancy in the mid-to-lower troposphere, leading to continental convective vigor (Matsui et al., 2020).

It is also hypothesized that the low-altitude concentrated cumulus thermal trains could additionally enhance the cold precipitation process by improving the residence time of graupel and hail within the mixed-phase zone if thermal-spilled graupel and hail encounter subsequent new cumulus thermals. Previous trajectory modeling (Heymsfield 1983) also suggested a similar mechanism for enhancing graupel and hail residence time and growth by multiple convective cores. Heymsfield (1983) used the multi-Doppler technique to generate a three-dimensional wind field, but it needed more spatio-temporal resolution to characterize cumulus thermal. However, a stronger updraft core mentioned in his study must be cumulus thermals. This investigation further requires a more complex set of numerical simulations in the future.

The proposed thermal-driven invigoration process is based solely on thermodynamics and does not consider aerosols' effect on deep convection, as demonstrated by previous studies over the Amazon (William et al. 2002, Lin et al. 2006). Our choice of single-moment microphysics does not consider the variability of background aerosols to initiate cloud droplets. However, this simple microphysics can generate a fundamental dry-wet contrast characterized by the V_{dop} statistics. This suggests that thermodynamics is the primary factor determining convective vigor, while aerosols may have a significant but secondary role in invigorating convection (Matsui et al. 2020). Future studies will require a higher-order moment of microphysics scheme to examine the impact of aerosols on droplet and primary ice nucleation in thermals to confirm our hypothesis that dry-wet aerosol contrast plays a secondary role.

https://doi.org/10.5194/egusphere-2024-3
Preprint. Discussion started: 26 January 2024

The proposed process for graupel-hail generation and convective vigor is a time-dependent, sequential, coupled dynamics-microphysics process. This process is not linear and cannot be adequately represented by the traditional convective mass flux method (Arakawa and Schubert 1974). To represent this process, thermal chain concepts with detailed microphysics processes must be introduced in the parameterization for large-scale models (Morrison et al., 2020). Fine-resolution simulations produce better continental convective vigor because they can resolve thermal dynamics and microphysics (Robinson et al., 2011; Matsui et al., 2020). The mean radius of the tracked thermal in this study, conducted using a 200 m mesh LES, is around 1 km, with a maximum size of around 2 km, which is comparable to the LES study using a 65-m horizontal grid spacing (Hernandez-Deckers and Sherwood, 2016). However, due to the effective resolution being 5-10 times the actual grid spacing, cumulus thermals, and graupel-hail generation processes are difficult to resolve for storm-resolving models and perhaps any Eulerian-type numerical atmospheric models (Matsui et al., 2016). Conducting LES for regional and global weather and climate models is impractical in the foreseeable future. Therefore, new types of dynamics-microphysics-coupled cumulus thermal parameterization should be developed to better represent deep convection for storm-resolving and coarse-resolution weather and climate models.

New ground-based Doppler phased array radar (PAR) technology (Kollias et al. 2022b) or multi-Doppler agile scans (Kollias et al. 2022a) hold promise in observing and characterizing cumulus thermals. Emerging PAR instruments have started capturing storm motion and microphysical details at spatial and temporal resolutions akin to those seen in LES output (e.g. Takahashi et al. 2019, Kikuchi et al. 2020). These new observational capabilities are necessary for refining the dynamics and microphysics in LESs, particularly in elucidating the process behind thermal-driven convective vigor. Moreover, the advent of vertical motion estimates from high-resolution space-based radars [EarthCARE, Wehr et al. 2023; Investigation of Convective Updrafts (INCUS), https://incus.colostate.edu; the Atmosphere Observing System (AOS), https://aos.gsfc.nasa.gov) will soon enable the global mapping of convective updrafts. These new satellite radar measurements will generate a comprehensive global catalog detailing convective vigor and the speed of intense thermals.

https://doi.org/10.5194/egusphere-2024-3
Preprint. Discussion started: 26 January 2024

Code Availability. The GCE LES code, G-SDSU simulator code, and Python plotting codes used in this mansucript are all available in the NCCS Data Portal (https://portal.nccs.nasa.gov/datashare/cloudlibrary/PUB_DATA/GoAmazon_ACP/Code/).

Data Availability. The RWP measurements and VARNAL LSF data were available from the Atmospheric Radiation Measurement (ARM) ARM Data Discovery (https://adc.arm.gov/discovery/#/). These data were obtained from the ARM Mobile Facility (AMF) at Manacapuru, Amazonas, Brazil, funded by A. U.S. Department of Energy (DOE) Office of Science User Facility managed by the Biological and Environmental Research program. The analysis data used in this manuscript is also available in the NCCS Data Portal (https://portal.nccs.nasa.gov/datashare/cloudlibrary/PUB_DATA/GoAmazon_ACP/Data/)

Author contribution. T. Matsui designed and performed the GCE LESs, the V_{dop} forward simulation, and the thermal tracking. D. Hernandez-Deckers developed the thermal tracking and analysis code for the GCE LESs and prepared the V_{dop} figures for the thermal analysis. S. Giangrande and T. Biscaro prepared RWP V_{dop} analysis. T. Matsui prepared the manuscript with contributions from all co-authors.

Competing interests. At least one of the (co-)authors is a member of the editorial board of Atmospheric Chemistry and Physics.

Acknowledgments. This project is funded by the NASA CloudSat and CALIPSO Science Team (CCST) program (program manager: Dr. David Considine, grant number: 80NSSC21K1135). The development of GCE is funded by the NASA GSFC Strategic Science resources (Associate Director for Institutional Planning and Operation: Dr. Karen Mohr). We also thank the NASA Advanced Supercomputing (NAS) Division and Center for Climate Simulation (NCCS) (Project Manager T. Lee at NASA HQ) for providing the computational resources to conduct the GCE and G-SDSU simulations, thermal tracking analysis, and stored model outputs. The authors thank an anonymous reviewer for improving the manuscript.

https://doi.org/10.5194/egusphere-2024-3
Preprint. Discussion started: 26 January 2024

References

Arakawa, A. and Schubert, W. H. (1974): Interaction of a cumulus cloud ensemble with the large–scale environment, Part I, J. Atmos. Sci., 31, 674–701.

Biscaro, T. S., Machado, L. A. T., Giangrande, S. E., and Jensen, M. P. (2021): What drives daily precipitation over the central Amazon? Differences observed between wet and dry seasons, Atmos. Chem. Phys., 21, 6735–6754, https://doi.org/10.5194/acp-21-6735-2021.

Blyth, A. M., S. G. Lasher-Trapp, and W. A. Cooper (2005): A study of thermals in cumulus clouds, Quarterly Journal of the Royal Meteorological Society, 131, 1171–1190, https://doi.org/10.1256/qj.03.180.

Chou, M.-D. and Suarez, M. J. (1999): A solar radiation parameterization for atmospheric studies, NASA Tech. Rep. NASA/TM-1999-10460, vol 15, p 38, https://ntrs.nasa.gov/archive/nasa/casi.ntrs.nasa.gov/19990060930.pdf.

Chou, M.-D. and Suarez, M. J. (2001): A thermal infrared radiation parameterization for atmospheric studies, NASA/TM-2001-104606, vol 19, p 55, https://ntrs.nasa.gov/archive/nasa/casi.ntrs.nasa.gov/20010072848.pdf.

Dolan, B., B. Fuchs, S. A. Rutledge, E. A. Barnes, and E. J. Thompson (2018): Primary Modes of Global Drop Size Distributions, J. Atmos. Sci., 75, 1453–1476, https://doi.org/10.1175/JAS-D-17-0242.1.

Emanuel, K. A., David Neelin, J., and Bretherton, C. S. (1994): On large-scale circulations in convecting atmospheres, Q. J. R. Meteorol. Soc., 120, 1111–1143, https://doi.org/10.1002/qj.49712051902.

Ghate, V. P. and Kollias, P. (2016): On the Controls of Daytime Precipitation in the Amazonian Dry Season, J. Hydrometeorol., 17, 3079–3097, https://doi.org/10.1175/JHM-D-16-0101.1.

Giangrande, S. E., Biscaro, T. S., and Peters, J. M. (2023): Seasonal controls on isolated convective storm drafts, precipitation intensity, and life cycle as observed during GoAmazon2014/5, Atmospheric Chemistry and Physics, 23, 5297–5316, https://doi.org/10.5194/acp-23-5297-2023.

Giangrande, S. E., Feng, Z., Jensen, M. P., Comstock, J. M., Johnson, K. L., Toto, T., Wang, M., Burleyson, C., Bharadwaj, N., Mei, F., Machado, L. A. T., Manzi, A. O., Xie, S., Tang, S., Silva Dias, M. A. F., de Souza, R. A. F., Schumacher, C., and Martin, S. T. (2017): Cloud characteristics, thermodynamic controls and radiative impacts during the Observations and Modeling of the Green Ocean Amazon (GoAmazon2014/5) experiment, Atmospheric Chemistry and Physics, 17, 14519–14541, https://doi.org/10.5194/acp-17-14519-2017.

Giangrande, S. E., Toto, T., Jensen, M. P., Bartholomew, M. J., Feng, Z., Protat, A., Williams, C. R., Schumacher, C., and Machado, L. (2016): Convective cloud vertical velocity and mass-flux characteristics from radar wind profiler observations during GoAmazon2014/5, Journal of Geophysical Research: Atmospheres, 121, 12,891–12,913, https://doi.org/10.1002/2016JD025303.

Giangrande, S. E., Wang, D., and Mechem, D. B. (2020): Cloud regimes over the Amazon Basin: perspectives from the GoAmazon2014/5 campaign, Atmospheric Chemistry and Physics, 20, 7489–7507, https://doi.org/10.5194/acp-20-7489-2020.

https://doi.org/10.5194/egusphere-2024-3
Preprint. Discussion started: 26 January 2024

Giangrande, S. E., E. P. Luke, and P. Kollias (2012): Characterization of Vertical Velocity and Drop Size Distribution Parameters in Widespread Precipitation at ARM Facilities, Journal of Applied Meteorology and Climatology, 51, 380–391, https://doi.org/10.1175/JAMC-D-10-05000.1.

Giangrande, S. E., S. Collis, J. Straka, A. Protat, C. Williams, and S. Krueger (2013): A Summary of Convective-Core Vertical Velocity Properties Using ARM UHF Wind Profilers in Oklahoma, Journal of Applied Meteorology and Climatology, 52, 2278–2295, https://doi.org/10.1175/JAMC-D-12-0185.1.

Grabowski, W. W. & Petch, Jon (2009): Deep Convective Clouds. Clouds in the Perturbed Climate System: Their Relationship to Energy Balance. 2. 197-215, https://doi.org/10.7551/mitpress/9780262012874.003.0009.

Gu, J.-F., Plant, R. S., Holloway, C. E., and Muetzelfeldt, M. R. (2020): Pressure drag for shallow cumulus clouds: From thermals to the cloud ensemble, Geophysical Research Letters, 47, e2020GL090460, https://doi.org/10.1029/2020GL090460.

Hartmann, D. L. (2016): Global Physical Climatology, 2nd ed., Academic Press, Cambridge, UK, ISBN: 978-0-12-328531-7, DOI: https://doi.org/10.1016/C2009-0-00030-0.

Hernandez-Deckers, D. and Sherwood, S. C. (2016): A Numerical Investigation of Cumulus Thermals, Journal of the Atmospheric Sciences, 73, 4117–4136, DOI: 10.1175/JAS-D-15-0385.1.

Hernandez-Deckers, D. and Sherwood, S. C. (2018): On the Role of Entrainment in the Fate of Cumulus Thermals, Journal of the Atmospheric Sciences, 75, 3911–3924, DOI: 10.1175/JAS-D-18-0077.1.

https://doi.org/10.5194/egusphere-2024-3
Preprint. Discussion started: 26 January 2024

Hernandez-Deckers, D., Matsui, T., and Fridlind, A. M. (2022): Updraft dynamics and microphysics: On the added value of the cumulus thermal reference frame in simulations of aerosol-deep convection interactions, Atmospheric Chemistry and Physics, 22(2), 711–724, DOI: 10.5194/acp-22-711-2022.

Heymsfield, A. J. (1983): Case Study of a Halistorm in Colorado. Part IV: Graupel and Hail Growth Mechanisms Deduced through Particle Trajectory Calculations, J. Atmos. Sci., 40, 1482–1509, https://doi.org/10.1175/1520-0469(1983)040<1482:CSOAHI>2.0.CO;2.

Holland, G. J., John, L., McBride, R. K., Smith, D. J., Jasper, D., and Keenan, T. D. (1986): The BMRC Australian Monsoon Experiment: AMEX, Bulletin of the American Meteorological Society, 67(12), 1466-1472, doi: 10.1175/1520-0477(1986)067<1466:TBAMEA>2.0.CO;2.

Iguchi, T., Matsui, T., Tao, W., Khain, A., Phillips, V., Kidd, C., L'Ecuyer, T., Braun, S., and Hou, A. (2014): WRF-SBM simulations of melting layer structure in mixed-phase precipitation events observed during LPVEx, J. Appl. Meteor. Climatol., 53, 2710-2731, doi:10.1175/JAMC-D-13-0334.1.

Jeyaratnam, J., Luo, Z. J., Giangrande, S. E., Wang, D., & Masunaga, H. (2021): A satellite-based estimate of convective vertical velocity and convective mass flux: Global survey and comparison with radar wind profiler observations, Geophysical Research Letters, 48, e2020GL090675, https://doi.org/10.1029/2020GL090675.

Kanji, Z. A., Ladino, L. A., Wex, H., Boose, Y., Burkert-Kohn, M., Cziczo, D. J., & Krämer, M. (2017): Overview of Ice Nucleating Particles, Meteorological Monographs, 58, 1.1–1.33, DOI: 10.1175/AMSMONOGRAPHS-D-16-0006.1.

Keenan, T. D. and Carbone, R. E. (1992): A Preliminary Morphology of Precipitation Systems In Tropical Northern Australia, Q.J.R. Meteorol. Soc., 118: 283-326, https://doi.org/10.1002/qj.49711850406.

Kikuchi, H. et al. (2020): Initial observations for precipitation cores with X-band dual polarized phased array weather radar, IEEE Transactions on Geoscience and Remote Sensing, 58(5), 3657-3666, http://doi.org/10.1109/TGRS.2019.2959628.

Kollias, P., Luke, E. P., Tuftedal, K., Dubois, M., & Knapp, E. J. (2022): Agile Weather Observations using a Dual-Polarization X-band Phased Array Radar, 2022 IEEE Radar Conference (RadarConf22), New York City, NY, USA, pp. 1-6, doi: 10.1109/RadarConf2248738.2022.9764308.

Kollias, P., Luke, E., Tuftedal, K., Dubois, M., & Knapp, E. J. (2022): Agile weather observations using a dual-polarization X-band phased array radar, 2022 IEEE Radar Conf., New York, NY, IEEE, 1–6, https://doi.org/10.1109/RadarConf2248738.2022.9764308.

Kollias, P., & Coauthors (2022): Science Applications of Phased Array Radars, Bull. Amer. Meteor. Soc., 103, E2370–E2390, https://doi.org/10.1175/BAMS-D-21-0173.1.

Korolev, A., Heckman, I., Wolde, M., Ackerman, A. S., Fridlind, A. M., Ladino, L. A., Lawson, R. P., Milbrandt, J., and Williams, E. (2020): A new look at the environmental conditions favorable to secondary ice production, Atmos. Chem. Phys., 20, 1391–1429, https://doi.org/10.5194/acp-20-1391-2020.

Korolev, A. and Leisner, T. (2020): Review of experimental studies of secondary ice production, Atmos. Chem. Phys., 20, 11767–11797, https://doi.org/10.5194/acp-20-11767-2020.

https://doi.org/10.5194/egusphere-2024-3
Preprint. Discussion started: 26 January 2024

Lang, S. E., Tao, W.-K., Chern, J.-D., Wu, D., & Li, X. (2014): Benefits of a fourth ice class in the simulated radar reflectivities of convective systems using a bulk microphysics scheme, J. Atmos. Sci., 71, 3583–3612, https://doi.org/10.1175/JAS-D-13-0330.1.

Lin, J. C., Matsui, T., Pielke Sr., R. A., & Kummerow, C. (2006): Effects of biomass burning-derived aerosols on precipitation and clouds in the Amazon Basin: A satellite-based empirical study, Journal of Geophysical Research, 111, D19204, doi:10.1029/2005JD006884.

Lucas, C., Zipser, E. J., & Lemone, M. A. (1994): Vertical velocity in oceanic convection off tropical Australia, J. Atmos. Sci., 51, 3183–3193, doi:10.1175/1520-0469(1994)051,3183: VVIOCO.2.0.CO;2.

Martin, S. T., & Coauthors (2017): The Green Ocean Amazon Experiment (GoAmazon2014/5) Observes Pollution Affecting Gases, Aerosols, Clouds, and Rainfall over the Rain Forest, Bulletin of the American Meteorological Society, 98, 981–997, DOI: 10.1175/BAMS-D-15-00221.1.

Matsui, T., & Mocko, D. M. (2014): Transpiration and Physical Evaporation: Regional and Seasonal Variability Over the Conterminous United States, In Encyclopedia of Natural Resources, 1st Ed.; Wang, Y. Q., Ed.; Taylor & Francis Group: New York. 1086pp, ISBN 9781439852583 - CAT# K12418.

Matsui, T., & Coauthors (2014a): Current and Future Perspectives of Aerosol Research at NASA Goddard Space Flight Center, BAMS Meeting Summary 95, ES203–ES207, doi: http://dx.doi.org/10.1175/BAMS-D-13-00153.1.

Matsui, T., & Coauthors (2014b): Introducing multisensor satellite radiance-based evaluation for regional Earth System modeling, Journal of Geophysical Research, 119, 8450–8475, doi:10.1002/2013JD021424.

Matsui, T., & Coauthors (2016): On the land-ocean contrast of tropical convection and microphysics statistics derived from TRMM satellite signals and global storm-resolving models, Journal of Hydrometeorology, 17, 1425-1445, doi:10.1175/JHM-D-15-0111.1.

Matsui, T., & Coauthors (2018): Impact of Radiation Frequency, Precipitation Radiative Forcing, and Radiation Column Aggregation on Convection-Permitting West African Monsoon Simulations, Climate Dynamics, 1-21, https://doi.org/10.1007/s00382-018-4187-2.

Matsui, T., & Coauthors (2020): Polarimetric Radar Characteristics of Simulated and Observed Intense Convective Cores for a Midlatitude Continental and Tropical Maritime Environment, J. Hydrometeor., 21, 501–517, https://doi.org/10.1175/JHM-D-19-0185.1.

Matsui, T., & Coauthors (2023): Systematic validation of ensemble cloud-process simulations using polarimetric radar observations and simulator over the NASA Wallops Flight Facility, Journal of Geophysical Research: Atmospheres, 128, e2022JD038134, https://doi.org/10.1029/2022JD038134.

Morrison, H., Peters, J. M., Varble, A. C., Hannah, W. M., & Giangrande, S. E. (2020). Thermal Chains and Entrainment in Cumulus Updrafts. Part I: Theoretical Description. Journal of the Atmospheric Sciences, 77, 3637–3660. [DOI: 10.1175/JAS-D-19-0243.1]

Morrison, H., Jeevanjee, N., Lecoanet, D., & Peters, J. M. (2023). What controls the entrainment rate of dry buoyant thermals with varying initial aspect ratio?. Journal of the Atmospheric Sciences, [DOI: 10.1175/JAS-D-23-0063.1], in press.

https://doi.org/10.5194/egusphere-2024-3
Preprint. Discussion started: 26 January 2024

Morton, B. R., Taylor, G. I., & Turner, J. S. (1956): Turbulent gravitational convection from maintained and instantaneous sources. Proc. Roy. Soc. London, 234A, 1–23, https://doi.org/10.1098/RSPA.1956.0011.

Öktem, R., Romps, D. M., & Varble, A. C. (2023). No Warm-Phase Invigoration of Convection Detected during GoAmazon. Journal of the Atmospheric Sciences, 80, 2345–2364. [DOI: 10.1175/JAS-D-22-0241.1]

Peters, J. M., Morrison, H., Varble, A. C., Hannah, W. M., & Giangrande, S. E. (2020). Thermal Chains and Entrainment in Cumulus Updrafts. Part II: Analysis of Idealized Simulations. Journal of the Atmospheric Sciences, 77, 3661–3681. [DOI: 10.1175/JAS-D-19-0244.1]

Pielke, R. A. (2001). Influence of the spatial distribution of vegetation and soils on the prediction of cumulus convective rainfall. Rev. Geophys., 39, 151–177, doi:10.1029/1999RG000072.

Pope, M., Jakob, C., & Reeder, M. J. (2009). Regimes of the North Australian Wet Season. Journal of Climate, 22, 6699–6715. [DOI: 10.1175/2009JCLI3057.1]

Prein, A. F., Ge, M., Valle, A. R., Wang, D., & Giangrande, S. E. (2022). Towards a unified setup to simulate mid-latitude and tropical mesoscale convective systems at kilometer-scales. Earth and Space Science, 9. [DOI: 10.1029/2022EA002295]

Ramos-Valle, A. N., Prein, A. F., Ge, M., Wang, D., & Giangrande, S. E. (2023). Grid spacing sensitivities of simulated mid-latitude and tropical mesoscale convective systems in the convective gray zone. Journal of Geophysical Research: Atmospheres, 128. [DOI: 10.1029/2022JD037043]

https://doi.org/10.5194/egusphere-2024-3
Preprint. Discussion started: 26 January 2024

Robinson, F., Sherwood, S., Gerstle, D., Liu, C., & Kirshbaum, D. (2011). Exploring the land-ocean contrast in convective vigor using islands. J. Atmos. Sci., 68, 602–618, https://doi.org/10.1175/2010JAS3558.1.

Rocha, H. R., Goulden, M., Miller, S. D., Menton, M. C., Pinto, L. D. V. O., Freitas, H. C., & Figueira, A. M. S. (2004). Seasonality of water and heat fluxes over a tropical forest in eastern Amazonia. Ecol. Appl., 14, 22–32.

Romps, D. M., & Charn, A. B. (2015). Sticky Thermals: Evidence for a Dominant Balance between Buoyancy and Drag in Cloud Updrafts. J. Atmos. Sci., 72, 2890–2901, https://doi.org/10.1175/JAS-D-15-0042.1.

Sherwood, S. C., Hernández-Deckers, D., Colin, M., & Robinson, F. (2013). Slippery Thermals and the Cumulus Entrainment Paradox. Journal of the Atmospheric Sciences, 70, 2426–2442, [DOI: 10.1175/JAS-D-12-0220.1]

Steiner, M., Houze Jr., R. A., & Yuter, S. E. (1995). Climatological characterization of three-dimensional storm structure from operational radar and rain gauge data. Journal of Applied Meteorology, 34, 1978–2007.

Stephens, G. L., Vane, D. G., Boain, R. J., Mace, G. G., Sassen, K., Wang, Z., ... CloudSat Science Team (2002). The CloudSat mission and the A-Train: A new dimension of space-based observations of clouds and precipitation. Bull. Amer. Meteorol. Soc., 83, 1771-1790, doi:10.1175/BAMS-83-12-1771.

Stolz, D. C., Rutledge, S. A., & Pierce, J. R. (2015). Simultaneous influences of thermodynamics and aerosols on deep convection and lightning in the tropics. J. Geophys. Res. Atmos., 120, 6207–6231, https://doi.org/10.1002/2014JD023033.

https://doi.org/10.5194/egusphere-2024-3
Preprint. Discussion started: 26 January 2024

Sullivan, S. C., Voigt, A. (2021). Ice microphysical processes exert a strong control on the simulated radiative energy budget in the tropics. Commun Earth Environ 2, 137, https://doi.org/10.1038/s43247-021-00206-7

Takahashi, H., Luo, Z. J., & Stephens, G. L. (2017). Level of neutral buoyancy, deep convective outflow, and convective core: New perspectives based on 5 years of CloudSat data. Journal of Geophysical Research: Atmospheres, 122(5), 2958-2969.

Takahashi, H., Luo, Z. J., & Stephens, G. L. (2021). Revisiting the entrainment relationship of convective plumes: A perspective from global observations. Geophys. Res. Lett., https://doi.org/10.1029/2020GL092349

Takahashi, N., et al. (2019). Development of multi-parameter phased array weather radar (MP-PAWR) and early detection of torrential rainfall and tornado risk. Journal of Disaster Research, 14(2), 235-247, http://doi.org/10.20965/jdr.2019.p0235

Tang, S., Xie, S., Zhang, Y., Zhang, M., Schumacher, C., Upton, H., Jensen, M. P., Johnson, K. L., Wang, M., Ahlgrimm, M., Feng, Z., Minnis, P., and Thieman, M. (2016). Large-scale vertical velocity, diabatic heating and drying profiles associated with seasonal and diurnal variations of convective systems observed in the GoAmazon2014/5 experiment. Atmos. Chem. Phys., 16, 14249–14264, https://doi.org/10.5194/acp-16-14249-2016.

Tao, W.-K., Lang, S., Zeng, X., Li, X., Matsui, T., Mohr, K., Posselt, D., Chern, J., Peters-Lidard, C., Norris, P. M., Kang, I.-S., Choi, I., Hou, A., Lau, K.-M., and Yang, Y.-M. (2014). The Goddard Cumulus Ensemble model (GCE): improvements and applications for studying precipitation processes. Atmospheric Research, 143, 392-424. doi: http://dx.doi.org/10.1016/j.atmosres.2014.03.005.

https://doi.org/10.5194/egusphere-2024-3
Preprint. Discussion started: 26 January 2024

Tao, W.-K., Wu, D., Lang, S., Chern, J.-D., Peters-Lidard, C., Fridlind, A., and Matsui, T. (2016). High-resolution NU-WRF simulations of a deep convective-precipitation system during MC3E: Further improvements and comparisons between Goddard microphysics schemes and observations. J. Geophys. Res. Atmos., 121, 1278–1305, https://doi.org/10.1002/2015JD023986.

Tokay, A., and Short, D. A. (1996). Evidence from Tropical Raindrop Spectra of the Origin of Rain from Stratiform versus Convective Clouds. Journal of Applied Meteorology and Climatology, 35, 355–371. [DOI: 10.1175/1520-0450(1996)035<0355:EFTRSO>2.0.CO;2]

Wang, D., Giangrande, S. E., Bartholomew, M. J., Hardin, J., Feng, Z., Thalman, R., and Machado, L. A. T. (2018). The Green Ocean: precipitation insights from the GoAmazon2014/5 experiment. Atmospheric Chemistry and Physics, 18, 9121–9145. [DOI: 10.5194/acp-18-9121-2018]

Wang, D., Giangrande, S. E., Schiro, K., Jensen, M. P., & Houze, R. A. (2019). The characteristics of tropical and midlatitude mesoscale convective systems as revealed by radar wind profilers. Journal of Geophysical Research: Atmospheres, 124, 4601–4619. [DOI: 10.1029/2018JD030087]

Wehr, T., Kubota, T., Tzeremes, G., Wallace, K., Nakatsuka, H., Ohno, Y., Koopman, R., Rusli, S., Kikuchi, M., Eisinger, M., Tanaka, T., Taga, M., Deghaye, P., Tomita, E., and Bernaerts, D. (2023). The EarthCARE mission – science and system overview. Atmos. Meas. Tech., 16, 3581–3608, https://doi.org/10.5194/amt-16-3581-2023.

Williams, E., and Stanfill, S. (2002). The physical origin of the land–ocean contrast in lightning activity. C. R. Phys., 3, 1277–1292, doi:10.1016/S1631-0705(02)01407-X.

https://doi.org/10.5194/egusphere-2024-3
Preprint. Discussion started: 26 January 2024

Williams, E., Chan, T., and Boccippio, D. (2004). Islands as miniature continents: Another look at the land–ocean lightning contrast. J. Geophys. Res., 109, D16206, doi:10.1029/2003JD003833.

Williams, E., Mushtak, V., Rosenfeld, D., Goodman, S., and Boccippio, D. (2005). Thermodynamic conditions favorable to superlative thunderstorm updraft, mixed phase microphysics and lightning flash rate. Atmos. Res., 76, 288–306, doi:10.1016/j.atmosres.2004.11.009.

Williams, C. R., Barrio, J., Johnston, P. E., Muradyan, P., and Giangrande, S. E. (2023). Calibrating radar wind profiler reflectivity factor using surface disdrometer observations. Atmospheric Measurement Techniques, 16, 2381–2398. [DOI: 10.5194/amt-16-2381-2023]

Wu, J., Del Genio, A. D., Yao, M.-S., and Wolf, A. B. (2009). WRF and GISS SCM simulations of convective updraft properties during TWP-ICE. Journal of Geophysical Research, 114, D04206. [DOI: 10.1029/2008JD010851]

Xie, S., Cederwall, R. T., and Zhang, M. (2004). Developing long-term single-column model/cloud system–resolving model forcing data using numerical weather prediction products constrained by surface and top of the atmosphere observations. J. Geophys. Res., 109, D01104, doi:10.1029/2003JD004045.

Xu, X., Sun, C., Lu, C., Liu, Y., Zhang, G. J., and Chen, Q. (2021). Factors affecting entrainment rate in deep convective clouds and parameterizations. Journal of Geophysical Research: Atmospheres, 126, e2021JD034881. [DOI: 10.1029/2021JD034881]

https://doi.org/10.5194/egusphere-2024-3
Preprint. Discussion started: 26 January 2024

Yanai, M., Esbensen, S., and Chu, J. (1973). Determination of Bulk Properties of Tropical Cloud Clusters from Large-Scale Heat and Moisture Budgets. J. Atmos. Sci., 30, 611–627, https://doi.org/10.1175/1520-0469(1973)030<0611:DOBPOT>2.0.CO;2.

Yuter, S. E., and Houze Jr., R. A. (1995). Three-dimensional kinematic and microphysical evolution of Florida cumulonimbus. Part II: Frequency distribution of vertical velocity, reflectivity, and differential reflectivity. Monthly Weather Review, 123, 1941–1963.

Zipser, E. J., Liu, C., Cecil, D. J., Nesbitt, S. W., and Yorty, D. P. (2006). Where are the most intense thunderstorms on Earth? Bull. Amer. Meteor. Soc., 87, 1057–1071, doi:10.1175/BAMS-87-8-1057.

Zhang, M., and Lin, J. (1997). Constrained variational analysis of sounding data based on column-integrated budgets of mass, heat, moisture, and momentum: Approach and application to ARM measurements. J. Atmos. Sci., 54(11), 1503–1524, doi:10.1175/1520-0469(1997)054<1503:CVAOSD>2.0.CO;2.

Zhang, M., Lin, J., Cederwall, R. T., Yio, J. J., and Xie, S. C. (2001). Objective analysis of ARM IOP data: Method and sensitivity. Mon. Weather Rev., 129(2), 295–311, doi:10.1175/1520-0493(2001)129<0295:OAOAID>2.0.CO;2.

https://doi.org/10.5194/egusphere-2024-3
Preprint. Discussion started: 26 January 2024

Figures

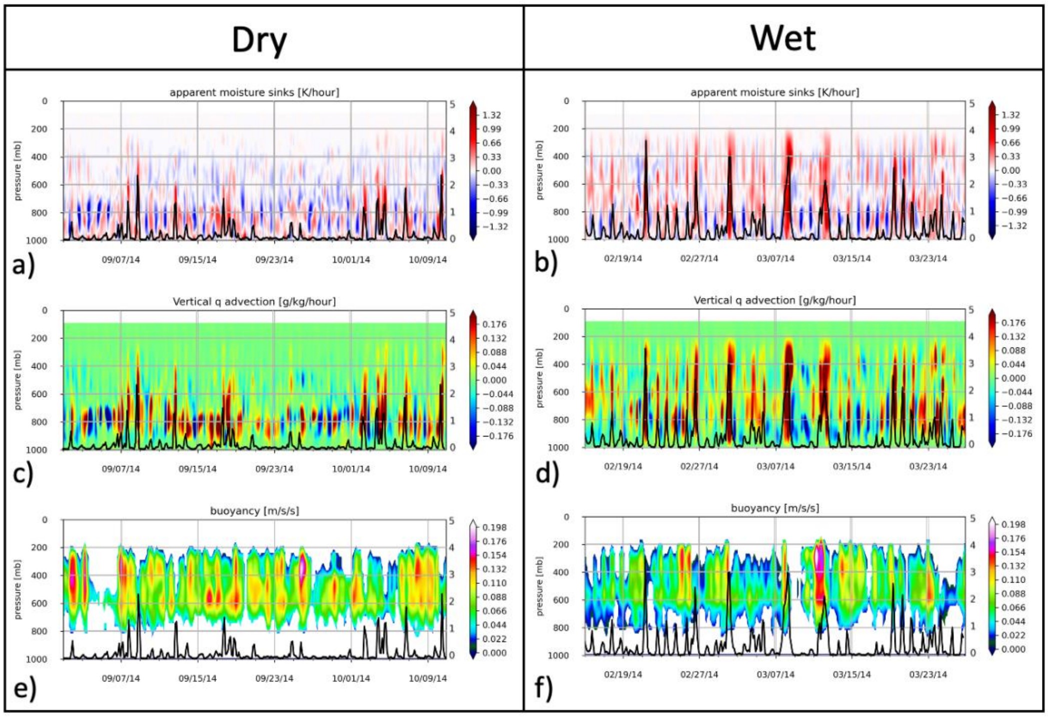

Figure 1. Time series of VARNAL large-scale forcing profiles between wet and dry periods: (a-b) apparent moisture sink (Q2), (c-d) vertical moisture advection, (e-f) potential buoyancy. The black solid lines on the secondary y-axis represent the surface precipitation rate.

https://doi.org/10.5194/egusphere-2024-3
Preprint. Discussion started: 26 January 2024

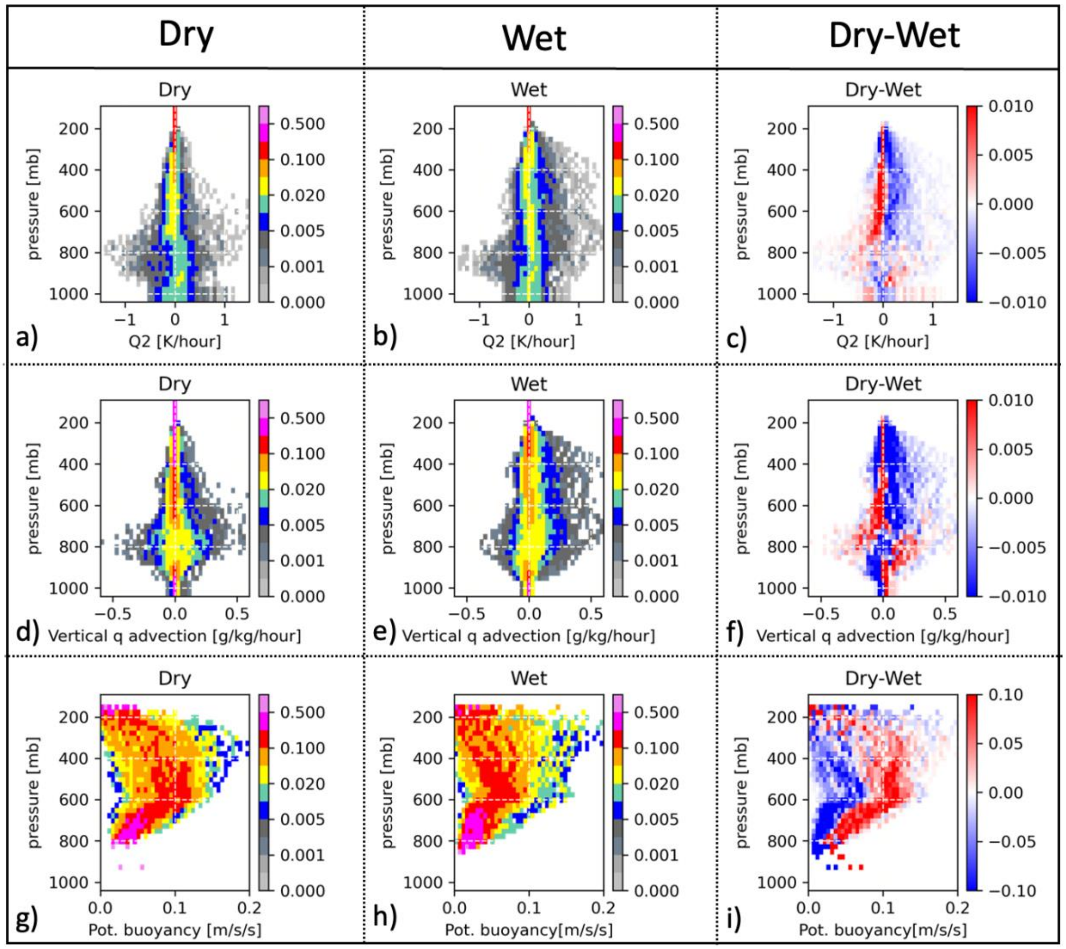

Figure 2. Contoured Frequency of Altitude Diagram (CFADs) of (a-c) apparent moisture sink (Q2), (d-f) vertical moisture (q) advection, (g-i) potential buoyancy integrated over dry and wet periods, as well as dry-wet differences.

https://doi.org/10.5194/egusphere-2024-3
Preprint. Discussion started: 26 January 2024

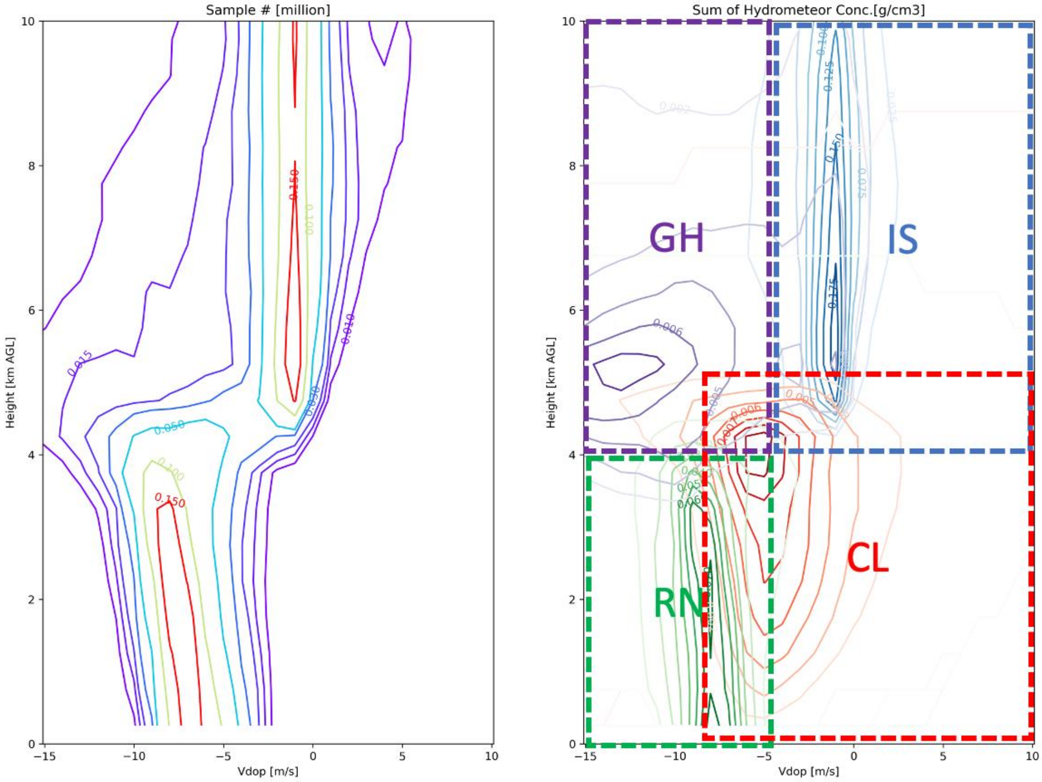

Figure 3. (a) Cumulative V_{dop} sample numbers from LESs during dry and wet periods, presented as CFADs for each V_{dop} bin and altitude. (b) the cumulative hydrometeor mass concentrations from each V_{dop}-altitude bin. Red contours represent "cloud (CL)", green contours represent "rain (RN)" blue contours represent "ice and snow (IS)", and purple contours represent "graupel and hail (GH)".

https://doi.org/10.5194/egusphere-2024-3
Preprint. Discussion started: 26 January 2024

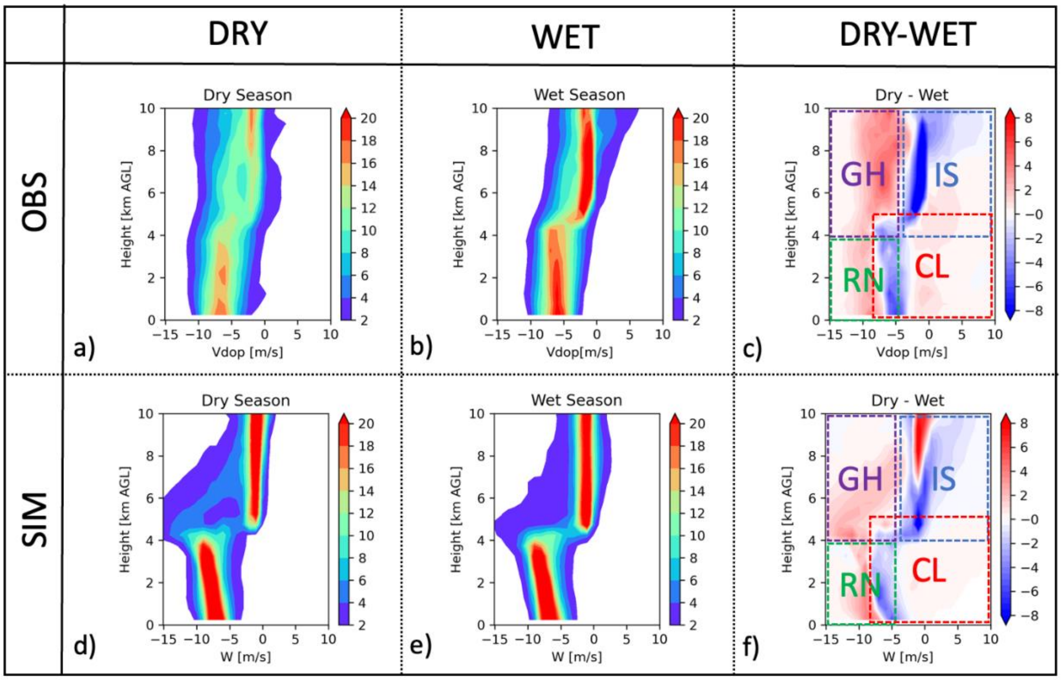

Figure 4. Contoured Frequency of Altitude Diagram (CFADs) of V_{dop} integrated over dry and wet periods, as well as dry-wet differences. The upper raw (a-c) represents observed composites, while the lower raw represents simulated composites. CL, RN, IS, and GH represent the hydrometeor regimes defined in Fig. 3.

https://doi.org/10.5194/egusphere-2024-3
Preprint. Discussion started: 26 January 2024

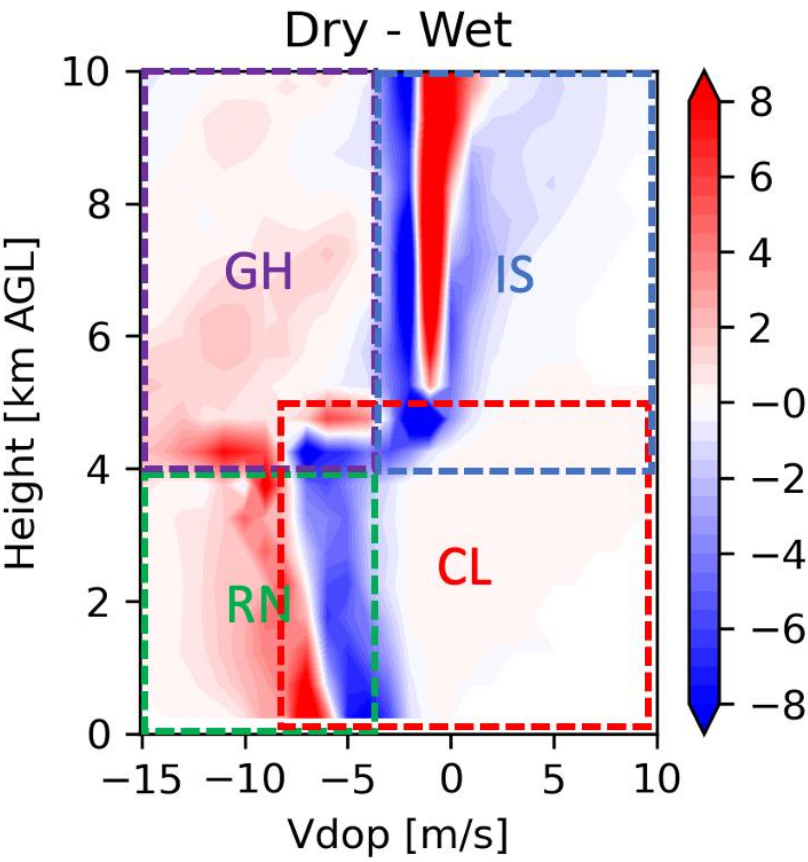

Figure 5. Contoured Frequency of Altitude Diagram (CFADs) of simulated V_{dop}, differentiated for dry- and wet-season golden cases.

https://doi.org/10.5194/egusphere-2024-3
Preprint. Discussion started: 26 January 2024

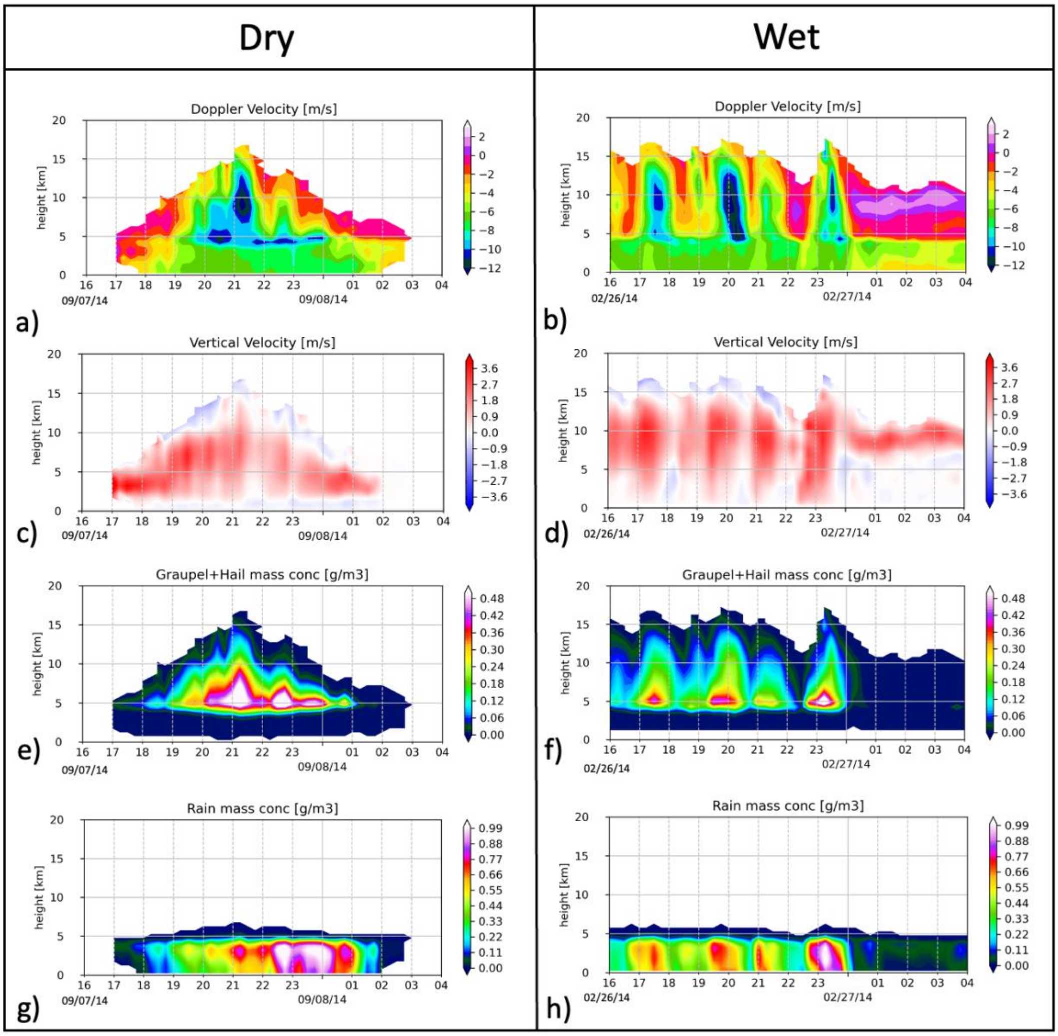

Figure 6. Time series of domain-mean (a-b) Doppler velocity, (c-d) vertical velocity, (e-f) graupel and hail concentrations, and (g-h) rain concentrations profiles of convective grids from the dry- and wet-season golden cases.

https://doi.org/10.5194/egusphere-2024-3
Preprint. Discussion started: 26 January 2024

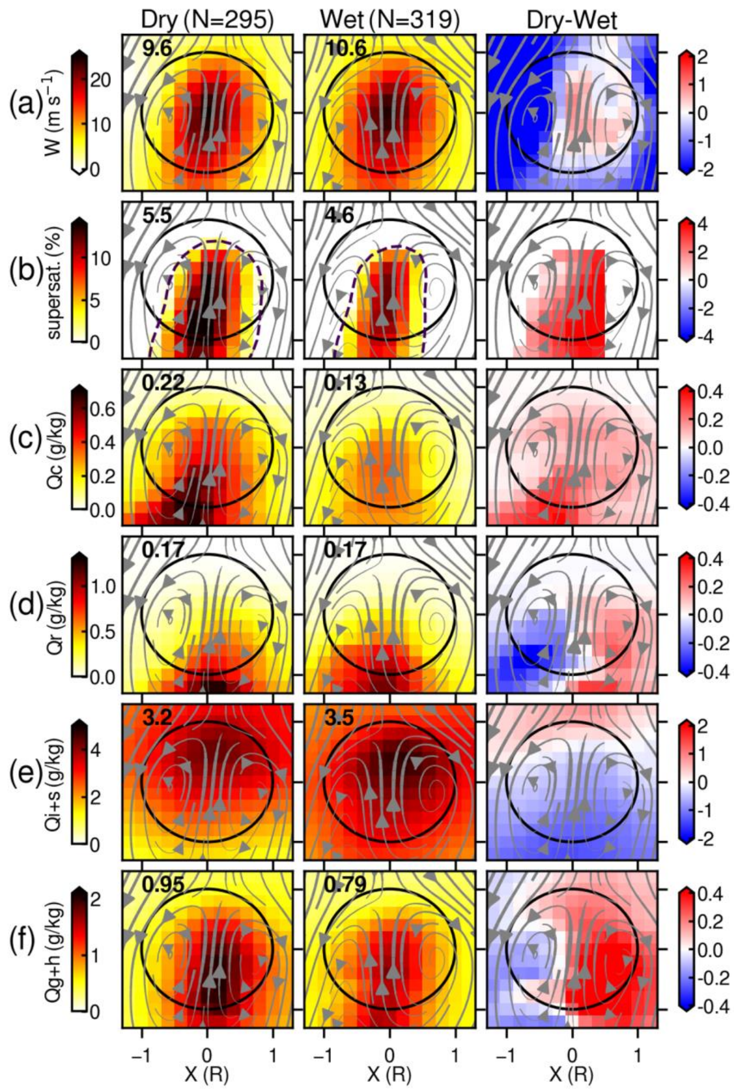

Figure 7. Cross sections along the x-z plane of flux-weighted thermal values of (a) vertical velocity (W), (b) supersaturation (S), (c) cloud droplet mass concentration (Qc), (d) rain mass concentration (Qr), (e) ice and snow mass concentration (Qi+s), and (f) graupel and hail mass concentration (Qg+h), for composites of all tracked thermals at the point of their maximum vertical velocity, scaled by their radius (horizontal and vertical coordinates are in units of mean thermal radii). Left, middle, and right column corresponds to the dry-season golden case, the wet-season golden case, and dry-wet case difference, respectively. Upper left values in each panel are the flux- and radius-weighted mean over all samples. Arrows indicate the average flow streamlines in the rising thermal reference frame. The dashed contour in supersaturation values corresponds to 100% relative humidity. These are reference-time (t=0) mean values.

https://doi.org/10.5194/egusphere-2024-3
Preprint. Discussion started: 26 January 2024

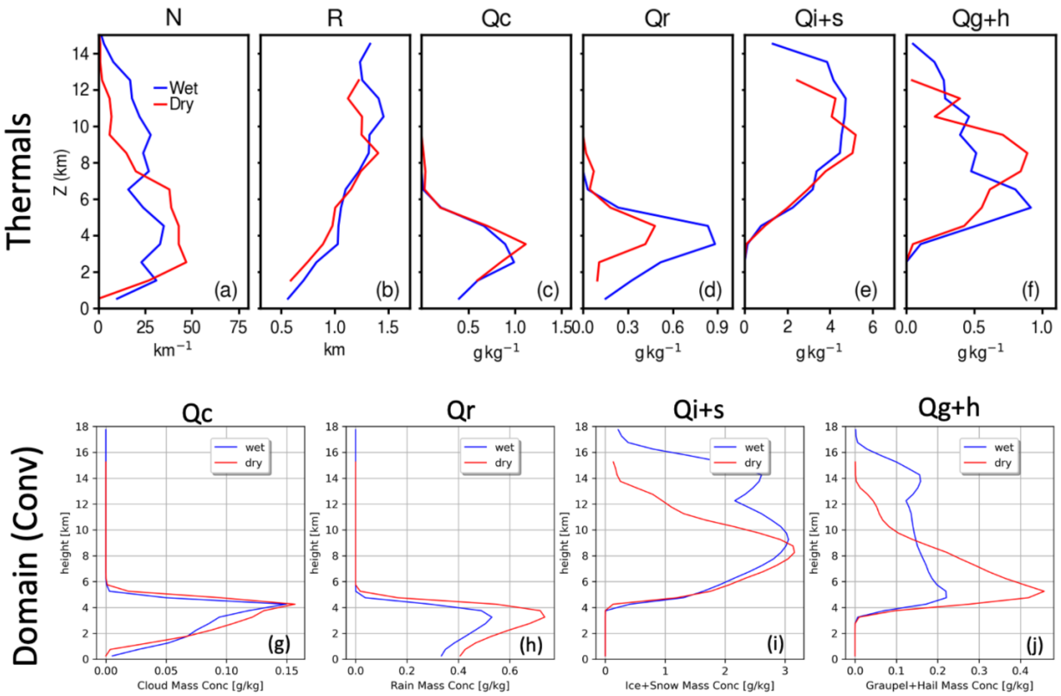

Figure 8. (a-f) Vertical profiles of thermal-mean (a) number concentrations, (b) radius, (c) cloud droplet mass concentration, (d) rain mass concentration (Qr), (e) ice and snow mass concentration (Qi+s), and (f) graupel and hail mass concentration (Qg+h). These are all-thermal mean values. (g-j) Vertical profile of domain-mean (g) cloud droplet mass concentration (Qc), (h) rain mass concentration (Qr), (i) ice and snow mass concentration (Qi+s), and (j) graupel and hail mass concentration (Qg+h) of convective grids from the dry- and wet-season golden cases.

https://doi.org/10.5194/egusphere-2024-3
Preprint. Discussion started: 26 January 2024

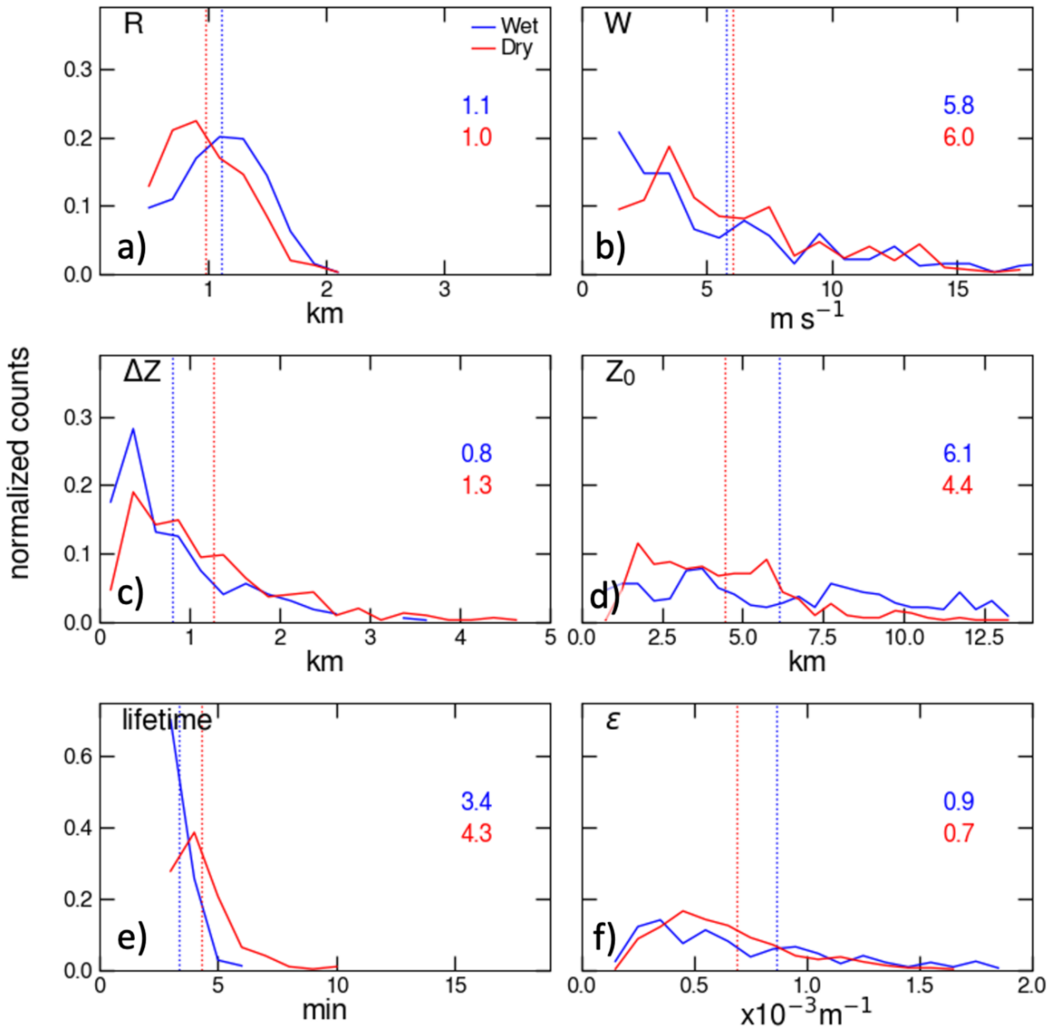

Figure 9. Normalized histogram of thermal (a) radii, (b) vertical velocity (W), (c) travel distance (DZ), (d) initiated level (Z_0), (e) lifetime, and (f) entrainment rate (e) from the dry- and wet-season golden cases.

https://doi.org/10.5194/egusphere-2024-3
Preprint. Discussion started: 26 January 2024

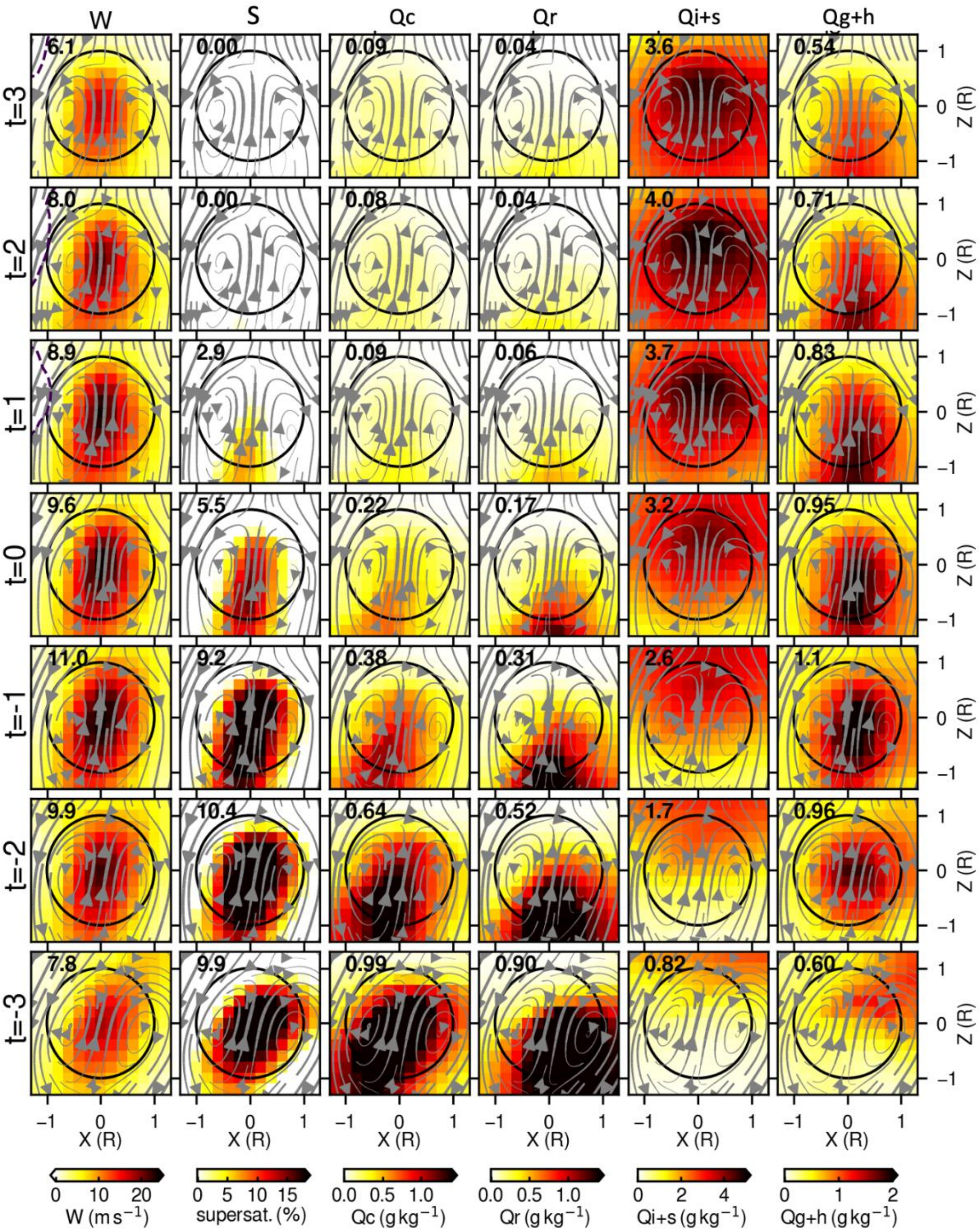

Figure 10. Time series of cross sections along the x-z plane of thermal mean values of vertical velocity, supersaturation values, cloud droplet mass concentration (Qc), rain mass concentration (Qr), (e) ice and snow mass concentration (Qi+s), and graupel and hail mass concentration (Qg+h), for composites of all tracked thermals scaled by their radius.

https://doi.org/10.5194/egusphere-2024-3
Preprint. Discussion started: 26 January 2024

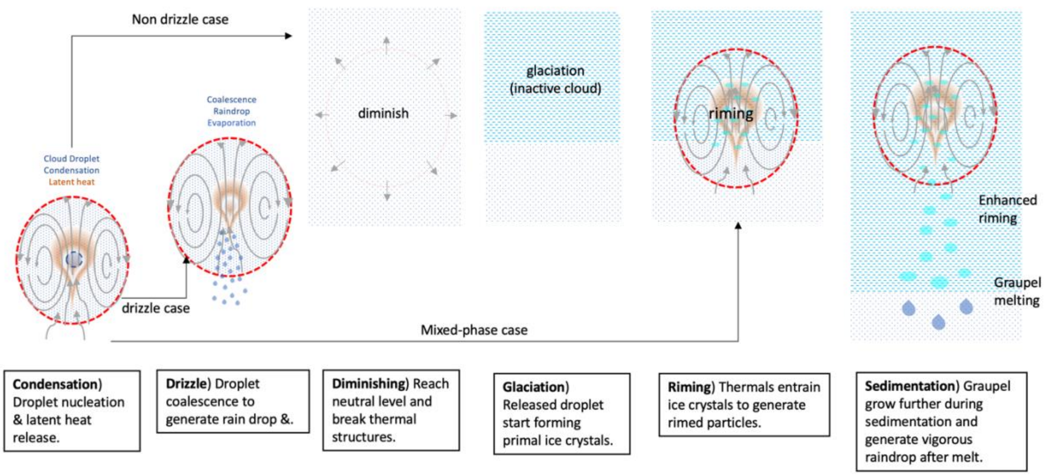

a)

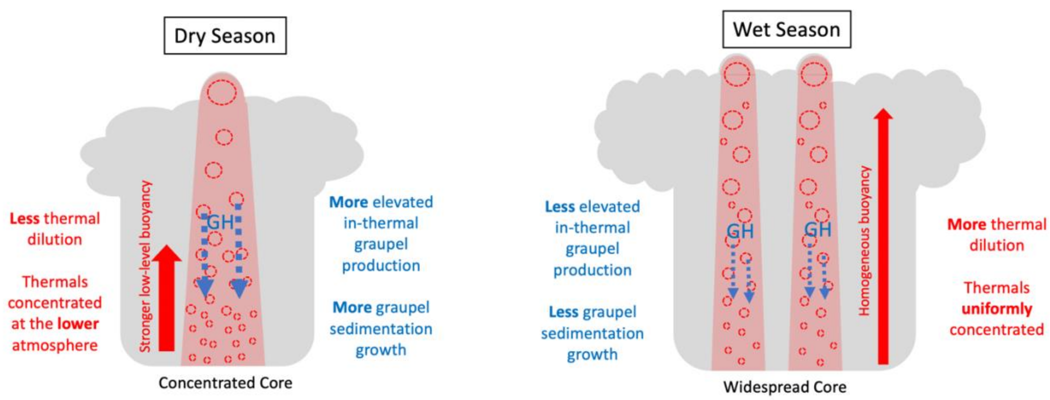

b)

Figure 11. (a) Diagram of the suggested mechanisms for generating graupel and hail through thermal processes. (b) Diagram of thermal characteristics in deep convection in the dry and wet seasons.